A MULTI-SATELLITE BASED TECHNIQUE FOR THE PHENOLOGICAL ASSESSMENT OF CYANOBACTERIAL ALGAL BLOOMS ACROSS INLAND WATERS

by

BENJAMIN PAGE

(Under the Direction of Deepak Mishra)

ABSTRACT

As the frequency of cyanobacterial harmful algal bloom (CyanoHABs) become more common across recreational and water supply lakes and reservoirs, demand for rapid detection and temporal monitoring will be imminent for effective management. This study demonstrated a multi-satellite based protocol for synoptic monitoring of rapidly evolving CyanoHABs across Earth's inland waters. The analysis involved a novel way to cross-calibrate a chlorophyll-*a* (Chl-*a*) detection model for NASA's Landsat-8 OLI sensor from the relationship between the normalized difference chlorophyll index (NDCI) and the floating algal index (FAI) derived from ESA's Sentinel-2A platform on a coinciding overpass date during the summer 2016 CyanoHAB bloom event in Utah Lake. This cross satellite–based monitoring method can be a great tool for regular monitoring and will reduce the budget cost for monitoring and predicting CyanoHABs in large lakes.

INDEX WORDS: CyanoHABs, FAI, Landsat-8, NDCI, Sentinel-2A, Water Quality

A MULTI-SATELLITE BASED TECHNIQUE FOR THE PHENOLOGICAL ASSESSMENT OF CYANOBACTERIAL ALGAL BLOOMS ACROSS INLAND WATERS

by

BENJAMIN PAGE

B.S., University of Minnesota-Duluth, 2010

A Thesis Submitted to the Graduate Faculty of The University of Georgia in Partial Fulfillment of the Requirements for the Degree

MASTER OF SCIENCE

ATHENS, GEORGIA

2017

A MULTI-SATELLITE BASED TECHNIQUE FOR THE PHENOLOGICAL ASSESSMENT OF CYANOBACTERIAL ALGAL BLOOMS ACROSS INLAND WATERS

by

BENJAMIN PAGE

Major Professor: Deepak Mishra
Committee: Susan Wilde
Marguerite Madden

Electronic Version Approved:

Suzanne Barbour
Dean of the Graduate School
The University of Georgia
May 2017

ACKNOWLEDGEMENTS

I would like to thank my advisor, Dr. Deepak Mishra, and the committee members Dr. Susan B. Wilde and Dr. Marguerite Madden. The knowledge they have shared with me has been inexplicitly invaluable. Dr. Mishra has given me many opportunities to participate in his other projects and the freedom to express my own research interests which drove me to this thesis idea. Most of my knowledge of cyanobacteria stems from the teachings of Dr. Wilde, who has been more than encouraging with expressive interest to new ideas. Dr. Madden’s questions allowed me to grasp the big picture in terms of spatial thinking, and my geospatial techniques and critical problem solving skills would not be where they are without her. Additionally, the staff and students in CGR and the image processing laboratory, driving the motivation with a collection of collaborative discussions, cannot go unacknowledged, and also provided much needed moral support.

TABLE OF CONTENTS

LIST OF TABLES

LIST OF FIGURES

CHAPTER 1

INTRODUCTION

As the frequency of cyanobacterial harmful algal blooms (CyanoHABs) become more common in recreational lakes and water supply reservoirs, demand for rapid detection and temporal monitoring will be imminent for effective management. Concurrently, with the expanding constellations of both government and commercial imaging satellites, data availability will increase due to improved revisit time and resolution. As these large datasets become more easily accessible to the scientific community and resource managements, so will the demand for the information that can be extracted from them. Therefore, it is preemptive to develop cross-sensor calibration techniques and algorithms to promote user-friendly application when incorporating multiple space-borne sensors for increased temporal targeting. The ultimate goal of this study was to demonstrate a novel and potentially operational cross-satellite based protocol for synoptic monitoring of rapidly evolving and increasingly common CyanoHABs in inland waters.

Cyanobacterial harmful algal blooms (CyanoHABs) have been a major cause for concern in aquatic ecosystems around the globe. These blooms often consist of harmful cyanobacteria, a type of photosynthetic bacteria which produce hazardous compounds including neurotoxins and hepatotoxins capable of inducing severe gastroenteritis, liver failure, and even death (Greenfield *et al*., 2014). Annual blooms of cyanobacteria species in the Baltic Sea and in Lake Erie, Ohio are just two commonly known recurring examples (Hansson *and* Hakansson, 2007; Steffen *et al*., 2014). CyanoHABs are becoming increasingly frequent across inland waters from varying climatic regions making local, national, and global headlines. For example, the Indian River Lagoon (IRL) in Florida experienced a historic brown bloom and CyanoHAB in February-March (2016) causing the death of thousands of fish, leaving a foul odor throughout surrounding towns and hindering recreational activities (Florida Center for Investigative Reporting, 2016; www.fcir.org). Not so long after, in June, 2016, a state of emergency was declared in Florida coinciding with the massive CyanoHAB in Lake Okeechobee flowing into the St. Lucie Rive. Furthermore, CyanoTRACKER (cyanotracker.uga.edu), a citizen science project to raise awareness and community participation to report CyanoHABs, has reported over 100 large domestic and international blooms in 2016 alone.

Factors that ultimately lead to the formation of different types of algal blooms in inland waters have been investigated for years. Studies have shown the effects of anthropogenic eutrophication can be intensified in inland waters as a result of increased summer temperatures associated with frequent drought events that are followed by heavy rainfall (Ahn *et al*., 2002; Tyler *et al*., 2008). This hyper-eutrophic condition promotes a lake or pond with a certain susceptibility to experience planktonic (freely floating) algal blooms when combined with excessive Phosphorus (P) and Nitrogen (N) input from the surrounding watershed, to manifest these toxic, food-web disrupting CyanoHABs (Paerl, *et al*., 2014). Additionally, warming can selectively promote cyanobacterial growth because as prokaryotes, their growth rates are optimized at relatively high temperatures (Paerl *and* Paul, 2011), and according to an independent analyses conducted by NASA and the National Oceanic and Atmospheric Administration (NOAA), Earth's 2016 surface temperatures were the warmest since modern recordkeeping began in 1880 (NOAA/NASA, Annual Global Analysis for 2016). It is therefore no surprise to consider that the Earth's increasing temperature trend is providing an optimal niche for CyanoHABs across inland waters.

Effects from the presence of CyanoHABs can be both economically and environmentally challenging. While it is difficult to place a value on the maintenance of a natural ecosystems, there may be impacts on fisheries, agriculture and tourism. For example, in 1991, nine water storages in New South Wales, Australia that are used for recreation were affected by algal blooms, with an economic loss estimated at $1.2 million (Steffensen, 2008). Taking all coastal and inland water bodies into account, it has been estimated that the cost of monitoring for cyanobacteria and for contingency planning to deal with blooms in Australia is $8.7 million per year (Atech, 2000).

Currently, the most common form of detection and monitoring during a bloom event includes *in-situ* sampling and laboratory analysis (Randolph *et al*., 2008; Osswald *et al*., 2007; McElhiney *and* Lawton, 2004; Msagati *et al*., 2006). While traditional *in-situ* sampling methodologies can provide rapid, accurate information about the target and even discern individual cyanobacteria species, they are often considered laborious and time consuming. Additionally, data collected from field campaigns are mostly in the form of point data, and fails to capture (1) the spatial distribution of the bloom and (2) the magnitude of concentrations across the extent of the affected area. Airborne scanning for the detection, identification and mapping of algal species has provided a rapid alternative in which the spatial distribution of algal blooms could be observed (Jupp *et al*., 1994; Sengpiel, 2007; Mishra *et al*., 2009). However, imaging sensors aboard aircraft must be capable to perform bio-optical models necessary to quantify water quality parameters. Additionally, the organization responsible for the economic cost of fuel and pilot for temporal monitoring may just lead to a financial sink.

Albeit the advancements in remote sensing technology, utilizing satellite imagery on a fairly regular environmental disaster in such a large body of water is just simply not a common practice, particularly at a time when data from numerous high temporal resolution satellites are freely available. The lack of studies can also be attributed to the atmospheric correction errors often encountered in Case-2 turbid waters. Existing atmospheric correction methods often yield negative water-leaving radiances primarily because the water-column reflectance interferes with the atmospheric correction based on the 765 nm and 865 nm spectral bands (Gordon *and* Voss, 1999; Hu *et al*., 2000; Bailley *et al*., 2010; Dash *et al*., 2012). This issue served as the primary motivation to modify a previously developed atmospheric correction to be extrapolated to multiple space-borne imaging sensors specifically to provide accurate reflectance products for studies involving inland water quality monitoring.

1.1 Remote sensing of water quality parameters

Multi- and hyper-spectral imagery collected by space-borne satellite platforms have provided a valuable tool for rapidly assessing the spatial variability of inland water quality parameters over synoptic scales (Gould *and* Arnone, 1997). For example, concentrations of the parameters such as chlorophyll-a (Chl-*a*), suspended particulate matter (SPM), colored dissolved organic matter (CDOM), and water optical properties can be computed from the water-leaving radiance (L_w) retrieved by atmospheric correction procedures. These parameters are important for studying and understanding biological and biogeochemical processes, and monitoring land-water interactions (He *et al*., 2012). Satellite platforms such as the Indian Remote Sensing (IRS) satellite's Ocean Color Monitor (OCM) sensor, NASA's Sea-viewing Wide Field-of-view sensor (SeaWiFs), the MODerate resolution Imaging Spectrometer (MODIS) and ESA's Medium Resolution Imaging Spectrometer (MERIS, now decommissioned) are popular choices for studying water quality parameters due to their extensive swath and band configurations (O'Reilly *et al*., 2000; Hu *et al*., 2004; Antoine *et al*., 2008; Dash *et al*., 2012; Mishra *and* Mishra, 2011;

Kumar *et al*., 2016). However, their ability to retrieve optically active constituents (OACs) from small to moderately sized freshwater reservoirs and lakes are unrealistic due to their coarse spatial resolution. Nonetheless, these platforms have offered invaluable, rapid, and cost-effective information regarding the quality of ocean and coastal waters.

In order to focus in on smaller inland water bodies, satellite platforms with higher spatial resolution must be utilized (Dash *et al*., 2012). As multiple linear predictors, multi- and hyperspectral satellite sensors have attempted to model water quality parameters such as turbidity and algal pigment concentrations in freshwater lakes as far back as 1978 (Carpenter, 1983). Since then, more recent, higher resolution satellites have become operational in which collected imagery can be downloaded for free via online applications such as USGS EarthExplorer and Global Visualization View (GloVis). For example, the Sentinel-2A (S2A) satellite launched on June 23, 2015 by the European Space Agency (ESA) is an ideal candidate for monitoring inland water quality due to its localized swath width of 290km at 10-20 meter spatial resolution. Additionally, the MultiSpectral Imager (MSI) aboard S2A contains channels useful for water quality models developed to quantify Chl-*a* concentrations such as the floating algal index (FAI) (Hu, 2009) and normalized difference chlorophyll index (NDCI) (Mishra *and* Mishra, 2011). Similarly, the Operational Land Imager (OLI) aboard NASA's Landsat-8 (LS8) platform is a 9-band pushbroom multispectral sensor with a 30 m spatial resolution. S2A MSI and LS8 OLI sensor specifications in terms of spectral band-centers are very similar. Although the width of each band varies in MSI, the 30 nm bandwidth in the OLI sensor is stable. For aquatic applications, the improved spatial resolution of the MSI sensor (10, 20 m) with regards to OLI (30 m) allows for a better separation of small scale features, and allows the observation of smaller river inlets and ponds (Vanhellemont *and* Ruddick, 2016). This can aid in the routine targeting and monitoring of CyanoHAB susceptible aquatic ecosystems that may be difficult to access. After resampling MSI to match OLI 30 m spatial resolution, examination of the spectral patterns retrieved by these two sensors can be employed and cross-calibrated to increase temporal resolution for more frequent monitoring of water quality parameters.

1.2 Atmospheric correction over inland waters

Measurements of L_w spectrum have now become routine because of the need to calibrate and validate satellite ocean color models (Siegel *et al*., 2000). The inland aquatic ecosystems on the other hand comprise less than 1% of the Earth's surface, but often are among the most productive areas (Likens, 1975). Atmospheric correction errors with satellite imagery over these optically-complex waters using traditional ocean color platforms are often encountered as a result of this production (Jamet *et al*., 2011), and turbid water pixels often become flagged under common processing software due to autonomous land masking thresholds or the overcorrection of atmospheric aerosols.

The remote sensing reflectance (R_{rs}) is a fundamental parameter widely used for estimating water quality parameters or benthic properties, and is the ultimate goal of atmospheric correction of ocean color measurements (Ye *et al*., 2017). In order to accurately derive R_{rs} from satellite imagery, both scattering and absorption properties in the atmosphere must first be identified, quantified, and subsequently removed as the molecular scattering signal due to ozone and Rayleigh effects may constitute as much as 90% of the total top-of-atmosphere (TOA) signal for spectral bands from the blue to red (typically 443 to 670 nm) (Gordon, 1997; Mishra *et al*., 2005). Although computation of ozone and Rayleigh contributions are relatively straightforward and mainly depend on sun-sensor geometry and study area elevation (Vermote *et al*., 1997), several studies have attempted to characterize aerosol type ε, and in practice it is uncommon to find the solutions in one place (Dash *et al*., 2012; Hu *et al*., 2004).

Over Case-1 clear-waters, water-leaving radiance is negligible in the near-infrared (NIR) portion of the electromagnetic spectrum (EMS) because of strong absorption by water, thus, the radiance measured at these wavelengths is essentially the contributions from the atmosphere (Gordon and Wang, 1994). However, this assumption does not work over Case-2 turbid-waters as the NIR reflectance is influenced by the OACs in the water column (Dash *et al*., 2012). These materials (OACs) include detrital biological material and abiotic particulates such as suspended sediments (Siegel *et al*., 2000). As ε is determined by choosing clear-water sites within the water body based on minimum TOA radiances, applying an NIR-based aerosol correction method over turbid inland waters, therefore, would assume a constant ε over the entire scene (Hu *et al.*, 2000). Extrapolating those values to the visible (VIS) portion of the spectrum would thus overestimate the aerosol contributions in highly productive regions. Additionally, over a homogenous, highly productive inland water body, especially during an algal bloom or after an influx of sediments from excessive runoff, clear water pixels are difficult to find, and are often nonexistent. Even with plenty of clear water pixels present, ε has been found to vary spatially in nature, and for a water body with a large distance between a turbid and clear water pixel, a single value for ε may not be appropriate (Jiang *and* Wang, 2014; Vanhellemont *and* Ruddick, 2015). Dash *et al*., (2012) have shown the efficacy of the Hu *et al.* (2000) aerosol correction, originally developed for MODIS over Case-1 waters, by successfully extrapolating the NIR-based method to OCM sensor aboard Oceansat-1 launched by the Indian Space Research Organization (ISRO) in May, 1999. Their study highlighted the robustness of a newly generated code for an atmospheric correction algorithm that could work across multiple space-borne sensors.

Unlike the NIR-based aerosol correction, it has been demonstrated that the incorporation of the shortwave-infrared (SWIR) channels of both MODIS and OLI sensors to characterize aerosol contribution alleviates the issue of the OACs interfering with the L_w signal, which assumes a zero water-leaving radiance contribution in these wavelengths even in the most optically-complex waters (Vanhellemont *and* Ruddick, 2015). One distinct advantage of using the SWIR band pair is that no clear water pixels are necessary to determine the aerosol type, a crucial advantage over the NIR-based aerosol method. Thus, the remaining signal received by these bands after ozone and Rayleigh correction are the result of the multiple scattering of aerosols, and can be quantified on a pixel-by-pixel basis. Following these assumptions, this study further elaborates the flexibility of the Hu *et* al. (2000) aerosol correction across two recently launched sensors over Case-2 inland waters. A modification of the aerosol path radiance (L_a) calculation was made by substituting the minimum vector coefficients usually obtained from the clear-water based NIR method with the two SWIR image matrices. This not only relieves the contamination issue encountered when using the NIR bands in turbid regions, but also compensates for over and under-corrections when the NIR method miscalculates ε within each pixel.

Commercial, academic, and government applications such as ENVI (commercial), ACOLITE (academic) and SeaDAS (government, NASA) allow the user to perform complex atmospheric corrections and image enhancements on data from multiple satellite imaging spectrometers (ENVI, 2009). However, their ability to retrieve more localized values of water-leaving reflectance (ρ_w) remain unknown as the algorithms they incorporate comprise of a complex suite of programs which is difficult to modify as a user (Dash *et al*., 2012), and have not been validated for inland water quality parameters. The radiative transfer calculations in these commercial applications apply traditional inversion models, using artificial neural network (ANN) techniques (Schroeder *et al*., 2007), and often fail to deliver accurate local parameters as such assumptions can promote errors in estimating surface reflectances (Bernardo *et al*., 2017). Therefore, rather than relying on a single software with built in functions that are uncontrollable to the researcher, a site specific, Modified Atmospheric correction for INland waters (MAIN) for the MSI and OLI sensors was developed using open-source applications to characterize unknown local variables such as ozone optical depth and site elevation. This potentially operational algorithm is anticipated to be utilized by lake resource managers to alleviate the issues encountered during the remote sensing of inland waters for accurate retrieval of water quality parameters.

1.3 Case study – Utah Lake

In this study, the MAIN algorithm was performed on two satellite images of Utah Lake acquired by S2A MSI and LS8 OLI which shared a coinciding overpass date on August 4th 2016 amidst a known CyanoHAB. The infamous summer 2016 bloom event hospitalized more than 100 people as a result from coming into contact with the water (The Guardian, Jul. 2016), which forced authorities to close the name-state lake for the first time in history (UDWQ, 2016). Thus far, only a single investigation of this phenomenon has incorporated a space-borne imaging platform to show the extent of an algal bloom using Earth Resources Technology Satellite (ERTS-1) in Utah Lake (Strong, 1974). However, Strong (1974) only showed the spatial patterns of the bloom distribution based on reflective properties in the green, red, and near-infrared (NIR) wavelengths using a single image date (September 12, 1972). Considering the lack of knowledge regarding multispectral bio-optical algorithms at that time, quantification of water quality parameters was absent. Therefore, quantification and a thorough phenological assessment of the 2016 bloom even in Utah Lake was investigated by constructing a time-series analysis of satellite derived Chl-*a* concentrations calibrated with *in-situ* cyanobacterial cell density (CCD) counts from UDEQ field campaigns.

CHAPTER 2

MATERIALS AND METHODS

2.1 Study area

Positioned in north-central Utah, USA at an altitude of 1,368 meters above sea level, surrounded by the Traverse Mountains and located between 40ºl4'42"N and 111º47'51"W. Utah Lake, a remnant of a much larger Pleistocene lake called Lake Bonneville, is a shallow (mean depth: 3 m) freshwater lake with a complex ecosystem which covers about half of Utah Valley's floor with a surface area of roughly 390 km^2 (Meritt, 2014) (Figure 1). The Utah Lake bed is flat as a result from 65,000 years of sediment build-up, creating a lacustrine pain over Utah Valley causing the lake to be so shallow (Jackson *and* Stevens, 1981). Utah Lake is highly eutrophic in nature and historically known for summer algae blooms, often consisting of toxic cyanobacteria species such as *Aphanizomenon flos-aquae*, *Dolichospermum crissum*, *Geitlerinema spp*. (I-III), *Microcystis aeruginosa*, *Oscillatoria princeps*, and *Pseudanabaena spp.* (UDEQ, 2016). In July 2016, a massive cyanobacterial bloom comprised primarily of *Aphanizomenon flos-aquae* spread across Utah Lake. Prior to the bloom event, June (2016) was already declared the hottest June on record for the United States (https://www.ncdc.noaa.gov/sotc/global/201606), part of a growing pattern of 14 straight months of high temperature records. It is well established that cyanobacteria are adapted to warmer temperatures where they are able to outcompete other phytoplankton groups (e.g, diatoms, cryptophytes, etc.) (Paerl *and* Otten, 2013), and therefore future blooms are highly probable. It has been documented that waste water discharge into Utah Lake from surrounding treatment plants can constitute up to 80% of the lake's total phosphorous input. However, local organizations are not sure that removal of phosphorous can control the bloom in the future, and for this purpose a long-term study will be underway to determine how much phosphorous the lake can handle without showing any adverse effect (Utah Lake Water Quality Study (2015-2019), UDEQ).

Satellite imagery of Utah Lake during the coinciding overpass of S2A MSI and LS8 OLI was collected from EOS Land viewer online application, which provides complete, free and open access to S2A MSI and LS8 OLI user products in Universal Transverse Mercator (UTM) projection with the WGS84 datum. Prior to implementing bio-optical models on the raw image products, upper atmospheric noise was first reduced by correcting the input bands for ozone and Rayleigh scattering effects. The input bands required in this study were based on the models chosen to visualize and quantify the extent of the CyanoHABs within Utah Lake and are given in Table (1). These models included the FAI originally developed by Hu (2009) for MODIS, and NDCI, developed by Mishra *and* Mishra (2011) for MERIS like sensors. Chl-*a* concentrations were estimated as it is considered to be a proxy for the detection of all algal biomass using a polynomial relation between NDCI values and *in-situ* measured Chl-a (R^2 = 0.95) from Mishra *and* Mishra (2011). The models are specifically designed to monitor and quantify the spatial distributions and concentrations of algal blooms, and can potentially assist lake resource managers for rapid bloom monitoring.

2.2 Modified atmospheric correction for inland waters (MAIN)

In ocean color remote sensing, the total radiance received by a satellite sensor in orbit over a water body (L_{TOA}) can be categorized from the contributions of Rayleigh scattering (L_{rc}), the multiple scattering of aerosols (L_{am}), transmittance effects (t), and the desired water-leaving radiance (L_w):

$$L_{TOA} = L_r + L_{am} + L_g + L_w(t) \quad (1)$$

Therefore, in an attempt to accurately model ρ_w and R_{rs} values over an inland water body, the logic of Equation (1) is assumed to hold true. The variable L_g, the radiance of the direct solar beam, i.e., photons that are specularly reflected from the water surface causing sun-glint is generally ignored because ocean-color sensors are equipped with a provision for tilting the scan plane away from the specular angle of the sun (Gordon *and* Wang, 1994). However, nadir-viewing sensors like MSI and OLI are susceptible to experience sun-glint effects depending on the sun-sensor geometry of the scene, and were instead masked out.

Ancillary data consisting of scene specific physical parameters needed to be known before further processing. Conveniently, both MSI and OLI satellite image products provide a metadata file (.xml for MSI, .MTL for OLI) which include important variables such as solar elevation, azimuth and zenith angles, satellite azimuth and zenith angles, and Earth-sun distance needed for Rayleigh contribution calculations. Raw OLI metadata provides multiplicative and additive coefficients for the radiometric correction process to convert the RAW 16-bit DN formatted images into TOA radiance or reflectance values.

Lastly, maximum radiance and reflectance values are embedded within the metadata for manual calculation of the extraterrestrial solar irradiance (F_0) across the available bands.

LS8 OLI Level-1C 16-bit DN format product over Utah Lake on August 4th, 2016 was first radiometrically calibrated using the radiance multiplicative (M_L) and additive (A_L) rescaling coefficients provided in the product metadata file using the following formula (USGS, http://landsat.usgs.gov/Landsat8_Using_Product.php):

$$L_{TOA\text{-}OLI} = M_L \times Q_{cal} + A_L \quad (2)$$

where $L_{TOA\text{-}OLI}$ is the TOA spectral radiance (W/(m^2 * sr * μm)) measured by the OLI sensor, and Q_{cal} is the quantized and calibrated standard product pixel values (DN).

Similarly, MSI Level 1C product was first converted from the provided TOA reflectance (ρTOA_{MSI}) into TOA radiance ($L_{TOA\text{-}MSI}$):

$$L_{TOA\text{-}MSI} = (\rho TOA_{MSI}(\lambda_i) \times F0'(\lambda_i) \times \cos(\theta_0)) / (\pi \times d^2) \quad (3)$$

The MAIN algorithm considers the effects from three fundamental atmospheric scattering parameters: ozone, Rayleigh and aerosols, and each scattering effect was addressed in order. Once the RAW imagery have been radiometrically calibrated, gaseous absorption from the ozone was removed from both TOA radiances of MSI and OLI imagery:

$$L_t^*(\lambda_i) = L_{TOA}(\lambda_i) \times e[\tau_{oz}(\lambda_i) \times (\cos(\theta_0)^{-1} + \cos(\theta_v)^{-1})] \quad (4)$$

where $L_t^*(\lambda_i)$ is the TOA radiance measured by the satellite sensor in the absence of ozone absorption effect (Hu *et al.* 2004), θ_0 is the solar zenith angle (degree), θ_v is the sensor zenith angle, and $\tau_{oz}(\lambda_i)$ is the ozone optical depth, calculated by following Gordon *et al.* (1999), and Mishra *et al.* (2005):

$$\tau_{oz}(\lambda_i) = k_{oz}(\lambda_i) \times DU / 1000 \quad (5)$$

where $k_{oz}(\lambda_i)$ is the ozone absorption coefficient taken from the Aerosol Optical Depth Value-Added Product (Koontz *et al.*, 2013) and DU is the ozone concentration in Dobson units obtained from NASA Ozone Over Your Head online application. This tool provides the total column ozone amount over any point on Earth for most dates between November 1978 and December 1994 and from August 1996 to today. This is not the amount of ozone that causes smog (tropospheric ozone), but rather a measure of ozone density through an entire column of atmosphere, from ground to space. The measurement is dominated by high altitude ozone (stratospheric ozone) (https://ozoneaq.gsfc.nasa.gov/tools/ozonemap/).

Subsequently, Rayleigh corrected radiances (L_{rc}) from TOA-ozone corrected bands of interest is computed as:

$$L_{rc}(\lambda_i) = L_t^*(\lambda_i) - L_r(\lambda_i), \quad (6)$$

where $L_r(\lambda_i)$ is the Rayleigh scattering contributions across each wavelength in radiance, and is defined by Gordon (1997):

$$L_r(\lambda_i) = F_0'(\lambda_i) \times \omega_{0r} \times \tau_r(\lambda_i) \times P_r / 4\pi \cos(\theta_v) \quad (7)$$

where F_0' is the extraterrestrial solar irradiance values (converted to $mW{*}cm^{-2} \cdot \mu m^{-1}$), P_r is the Rayleigh scattering phase function calculated by following Doerffer's (1992) logic, and ω_{0r} is the single scattering albedo ($\omega_{0r} = 1$). Finally, $\tau_r(\lambda_i)$ is the Rayleigh optical thickness and is defined by Hansen *and* Travis (1974) as:

$$\tau_r(\lambda_i) = \frac{P}{Po} \times [\, 0.008569\, \lambda_i^{-4} (1 + 0.0113\, \lambda_i^{-2} + 0.00013\, \lambda_i^{-4})] \quad (8)$$

where λ_i is each band's centered wavelength in μm, and P_0 is standard atmospheric pressure of 1,013.25 mb and P is the calculated pressure from the study area elevation (in meters). Study site elevation was acquired using Google Earth (unit: ft.) for altitude pressure calculations for Rayleigh contribution determination:

$$P = (101325 \times (1 - 2.25577E\text{-}5 \times \text{elevation})^{5.25588}) \times 0.01 \quad (9)$$

At large solar zenith angles, such as encountered in the analysis of high-latitude imagery, errors in Rayleigh reflectances can become quite large, e.g., >10% in the blue band (Gordon *et al*., 1988). Therefore, it is extremely important to consider the study site elevation for accurate R_{rs} retrieval. A digital elevation model (DEM) may also be used when correcting an entire image tile to compensate the differences in pressure changes respect to elevation on a pixel-by-pixel basis. Rayleigh corrected radiances were then converted back to reflectance following the USGS method (Landsat 8 User's Handbook):

$$\rho_{rc}(\lambda_i) = (\pi \times L_{rc}(\lambda_i) \times d^{2}) / (F_0' \times \cos(\theta_0)) \quad (10)$$

where *d* is the Earth-sun distance in the astronomical unit (AU) found within the OLI metadata .MTL file. Rayleigh corrected reflectances are useful in the ocean color community as the molecular scattering signal due to ozone and Rayleigh effects in the atmosphere may constitute as much as 90% of the total top-of-atmosphere (TOA) signal for spectral bands from the blue to red (typically 443 to 670 nm) (Gordon, 1997; Mishra *et al*., 2005). These bands are often incorporated into bio-optical algorithms used to derive the OACs from the water column, such as Chl-*a* biomass and suspended particulate matter (SPM), common products generated by the NASA Ocean Biology Processing Group (OBPG) for coastal and open ocean algal biomass.

Masking

After collecting $\rho_{rc}(\lambda_i)$, masking for clouds and sun-glint effects was performed in order to retrieve an accurate representation of the lake area without the interference of unrealistic values. A threshold value was set to the shortest of the middle infrared bands available on the OLI sensor (1609 nm) to 0.0215. In other words, pixels were masked if OLI $\rho_{rc}(1609) > 0.0215$. This simple threshold method works well throughout the world for discriminating water from floating objects, offshore constructions, land and clouds, even in extremely turbid waters (Vanhellemont *and* Ruddick, 2015). After resampling MSI spatial resolution from 20 m to 30 m, remaining MSI cloud and sun-glint free pixels were multiplied by the OLI water mask leaving n=138,814 pixels to be examined and compared against each other in a multispectral feature space.

Aerosol Correction

The strong impact of aerosols in the visible and near infrared spectral range can be difficult to correct, because they can be highly discrete in space and time (e.g., smoke plumes) and because of the complex scattering and absorbing properties of aerosols that vary spectrally and with aerosol size, shape, chemistry and density (Vermote *et al*., 2016). In this study, ε was determined by utilizing the two shortwave infrared (SWIR) channels available on both MSI and OLI: one to assess the magnitude of aerosol contribution (1610 nm for MSI, 1609 for OLI), and one to extrapolate to the bands that are within the visible part of the electromagnetic spectrum (EMS) (2190 nm for MSI, 2201 nm for OLI). Unlike using the NIR region of the EMS to determine aerosol type, in which pixels are highly sensitive to increased levels of OACs within the water column (Dash *et al*., 2012), both SWIR bands are assumed to have a zero marine contribution even in the most optically-complex waters (Vanhellemont *and* Ruddick, 2015). Therefore, after

Rayleigh and ozone correction, any signal received by the SWIR bands are the result from non-selective scattering from particles in the lower atmosphere that has a diameter less than the incident wavelengths (< 1609 nm). Aerosol path radiance ($L_a(\lambda_i)$) was first quantified by assuming an exponential relationship between aerosol optical thickness and wavelength (Gordon *and* Wang, 1994), and the phase function to remain constant over the desired wavelengths (Mohan *and* Chauhan, 2003):

$$L_a(\lambda) / F_0'(\lambda) = ke^{(-c\lambda)} \quad (11)$$

where *k* and *c* are constants. The assumption of a zero water leaving radiance contribution in the SWIR wavelengths allowed for the modification of Equation (11) by substituting $L_a(\lambda)$ values usually collected over the clear or open water regions with the two L_{rc} SWIR ($L_{rc}(\lambda_{SWIR\text{-}1})$ and $L_{rc}(\lambda_{SWIR\text{-}2})$ image matrices:

$$L_{rc}(\lambda_{SWIR\text{-}1}) / F_0'(\lambda_{SWIR\text{-}1}) = ke^{(-c\lambda)} \quad (12)$$

$$L_{rc}(\lambda_{SWIR\text{-}2}) / F_0'(\lambda_{SWIR\text{-}2}) = ke^{(-c\lambda)} \quad (13)$$

which leads to the natural logarithm of both equations:

$$Ln[L_{rc}(\lambda_{SWIR\text{-}1}) / F_0'(\lambda_{SWIR\text{-}1})] = k\,(-c)\,\lambda = -\,\varepsilon\lambda_{SWIR\text{-}1} \quad (14)$$

$$Ln[L_{rc}(\lambda_{SWIR\text{-}2}) / F_0'(\lambda_{SWIR\text{-}2})] = k\,(-c)\,\lambda = -\,\varepsilon\lambda_{SWIR\text{-}2} \quad (15)$$

Aerosol type ε was then determined for each pixel as the negative of the slope of the straight line between $\Delta\lambda_{SWIR\text{-}1,2}$ and $\Delta Ln[L_{rc}(\lambda_{SWIR\text{-}1,2}) / F_0'(\lambda_{SWIR\text{-}1,2})]$ as:

$$(Ln[L_{rc}(\lambda_{SWIR\text{-}2}) / F_0'(\lambda_{SWIR\text{-}2})] - Ln[L_{rc}(\lambda_{SWIR\text{-}1}) / F_0'(\lambda_{SWIR\text{-}1})]) / (\lambda_{SWIR\text{-}2} - \lambda_{SWIR\text{-}1}) = -\varepsilon \quad (16)$$

The output returns a raster distribution map of ε which was extrapolated to the visible region of the EMS on a pixel-by-pixel basis, rather than a single value (usually a median, mean, or mode) commonly retrieved in the clear-water pixel method described by Hu *et al.* (2000) which is responsible for unrealistic and/or negative-water leaving reflectances in highly productive waters. Extrapolating to the visible part of the EMS was then possible to create an aerosol radiance map (L_{am}) to quantify the aerosol contribution across each channel:

$$L_{am}(\lambda_i < 1609\ \text{nm}) = L_{rc}(\lambda_{SWIR\text{-}2}) \times (F_0' / F_0'(\lambda_{SWIR\text{-}2}))e^{[-\varepsilon\ (\lambda i\ /\ \lambda swir\text{-}2)]} \quad (17)$$

$L_{am}(\lambda_i)$ was then converted to reflectance (ρ_{am}) for $\rho_w(\lambda_i)$ and subsequent R_{rs} calculations by following Equation (10).

Remote sensing reflectance

Finally, once all the necessary variables are defined, the desired $\rho_w(\lambda_i)$ is calculated by:

$$\rho_w(\lambda_i) = \rho_{rc}(\lambda_i) - \rho_{am}(\lambda_i) / t(\lambda_i) \quad (18)$$

where $\rho_{rc}(\lambda_i)$ is the reflectance contribution from Rayleigh scattering, $\rho_{am}(\lambda_i)$ is the corresponding aerosol reflectance map at each wavelength, and $t(\lambda_i)$ is the diffuse transmittance from the water surface to the satellite, and is calculated as:

$$t(\lambda_i) = e^{[(-\tau r\ (\lambda i) / 2)\ (1 / \cos(\theta v))]} \quad (19)$$

For R*rs* calculation, $\rho_w(\lambda_i)$ is simply divided by π:

$$R_{rs}(\lambda_i) = \rho_w(\lambda_i) / \pi \quad (20)$$

The MAIN algorithm does not include out-of-band correction, whitecap correction, surface roughness influences and contribution of L_{am} to diffuse transmittance. However, these corrections will not significantly change the overall accuracy of the procedure particularly for small lakes or estuaries on low wind speed days when whitecap and surface roughness terms are minimal (Dash *et al*., 2012). Although *in-situ* measurements of atmospheric conditions over Utah Lake were not collected in the field, the input of parameters such as ozone optical depth, site elevation, and sun-sensor geometry is a viable approach for correcting the image and starting the iterative process made by scene specific atmospheric correction algorithms (Moses *et al*., 2012).

2.3 MAIN Performance – Utah Lake

In order to make sense of the derived R_{rs} values from the MAIN processed MSI and OLI images over Utah Lake, comparison with *in-situ* measurements is a common, standardized practice. Unfortunately, *in-situ* measurements of R_{rs} and atmospheric conditions of Utah Lake were not collected in the field during the coinciding MSI and OLI overpass on Aug. 4th, 2016. Meanwhile, the Utah Department of Environmental Quality (UDEQ) deploys sampling crews to collect general surface water parameters (temperature, DO, pH, etc.) and algal density for known cyanobacterial blooms. However, *in-situ* spectroradiometer measurements for R_{rs} or properties of the atmosphere in respect to aerosols are not considered. In the absence of any radiometric "ground" truth such as buoy or other suitable matchup data, an inter-comparison of satellite sensors is often the best choice (Suresh *et al*., 2006), but for smaller lakes and reservoirs, inter-comparison using larger scale satellites such as MODIS and Sentinel-3 is impractical as the reduced spatial resolution would not be able to accurately represent the distribution of water quality parameters, specifically near the lake boundaries where algal blooms are most common. Therefore, confidence in the atmospherically corrected values originated from performing the MAIN algorithm on another inland water body during a LS8 OLI overpass in Georgia, USA coinciding with fieldwork conducted two years prior on October 22nd, 2014. Thus, any error analysis between the MAIN derived R_{rs} values and *in-situ* measurements was only possible for the OLI sensor, as MSI was still under construction and had not launched yet.

2.4 MAIN validation

Lake Sinclair (33.19°, -83.28°) (Figure 2, bottom) is a multi-use freshwater inland reservoir created in 1953. Spanning across 6,200 hectares (ha) within the Georgia Piedmont, Lake Sinclair is the second largest reservoir in the state. In 1973, Georgia Power constructed the Wallace Dam on the Oconee River, separating Sinclair from its sister lake, Oconee (33.19°, -83.28°) (Figure 2, top). The Oconee River is the main source of water for this reservoir and supplies roughly 70% of the lake's water (Fisher *et al*. 1999). The lake is also fed by waters from the Apalachee River and several small creeks in the area. With average depths of 27 m (Sinclair) and 6.4 m (Oconee), Lake Sinclair and Lake Oconee together are considered oligotrophic lakes, with nutrient poor lake basins composed of sandy or rocky bottoms, and scarce bottom vegetation (Smith *and* Manoylov, 2013). However, intensified summer temperatures combined with heavy rainfall after severe drought effects can intensify anthropogenic eutrophication (Ahn, *et al*., 2002), and excessive Phosphorus (P) and Nitrogen (N) input from the surrounding watershed can promote a lake with a certain susceptibility to experience planktonic (freely floating) algal blooms often consisting of toxic-forming cyanobacterial species (Paerl *et al*., 2014). As the Georgia Piedmont is characterized by a warm and humid, temperate climate, the Lake Sinclair/Oconee pair have experienced isolated CyanoHABs where runoff is significant.

In-situ R_{rs} values were obtained with a hand-held GER-1500 (Spectra Vista, Co.) spectroradiometer on October 22nd, 2014 at 15 sites divided amongst 3 sampling locations (SL) in both Lake Oconee (SL1 and SL2) and Lake Sinclair (SL3) coinciding with cloud-free OLI data (Figure 2). The hyperspectral data were weighted with the relative spectral response function of OLI to yield R_{rs} values at the seven OLI wavelength bands (443, 483, 561, 655, and 865 nm) by following Mobley, (1999):

$R_{rs}(\theta, \varphi, \lambda, 0^{+}) = L_{u}(\theta, \varphi, \lambda, 0^{+}) - 0.028 \times L_{sky}(\theta,\varphi,\lambda,0+) \,/\, E_{d}(\theta,\varphi,\lambda, 0^{+})$ (21)

where L_u is the upwelling irradiance measured by the spectroradiometer, φ is the azimuthal angle (in 90 deg); θ is the zenithal angle (of 45 deg); λ is the wavelength (in nm), and 0^{+} indicates that radiance and irradiance measurements were acquired just above the water surface (Bernardo *et al*., 2017). Additionally, to remove the effect of sensor-specific spectral response from R_{rs}, full-band-pass water-leaving radiances were adjusted to that for square 11-nm band-passes located at the nominal band centers using the model of Werdell *and* Bailey., (2005) (Franz, 2014).

2.5 Performance evaluation of multiple atmospheric corrections

Several atmospheric correction algorithms exist (Berk *et al*., 1999; Adler-Golden *et al*., 1998; Matthew *et al*., 2000; Ruddick *et al*., 2000; Vanhellemont and Ruddick, 2015; Richter and Schläpfer, 2016), however, there is no consensus about which one should be used for remote sensing of the inland water color (Bernardo *et al*., 2017). This study further extends the comparisons between *in-situ* and modeled R_{rs} resulting from four commonly used atmospheric corrections seen by Bernardo *et al*., (2017) with the addition of the performance of the MAIN algorithm on an inland water body (Lake Oconee / Sinclair) in an humid subtropical climate. A brief description of the additional tested atmospheric corrections are provided in Table (2).

Performance of the resulting R_{rs} values over Lake Oconee / Sinclair derived from each atmospheric correction relative to the radiometric quantities collected in the field were statistically evaluated by a normalized root mean square error (*n*RMSE) at each wavelength:

$$RMSE = \frac{\sqrt{\sum_{i=1}^{n}[x_i(\lambda)-x_g(\lambda)]^2}}{n} \quad (22)$$

where x_i is the OLI atmospherically corrected R_{rs} pixel at band λ_i matching the geographic location of true R_{rs} obtained *in-situ* (x_g) by the GER-1500 spectroradiometer. It is important to note that while *in-situ* measurements are sometimes referred to as 'ground-truth' measurements, they are rarely 'absolute truth'. Full characterization of the inherent measurement error of the field instrument is essential for any validation effort (Bailey *and* Werdell, 2006). Nevertheless, standardizing Equation (22) further allows for a more comprehensible value:

$$nRMSE = \frac{RMSE}{x_{g_{max}} - x_{g_{min}}} \times 100 \quad (23)$$

Relative error analysis between MSI and OLI derived R_{rs} products for the Utah Lake images was conducted through mean absolute percent error (MAPE) in addition to *n*RMSE:

$$MAPE = \frac{1}{n} \times \sum_{i=1}^{n} \left| \frac{x_{MSI} - x_{OLI}}{x_{OLI}} \right| \times 100 \quad (24)$$

where x_{MSI} and x_{OLI} are the modeled R_{rs} resulting from the MAIN algorithm applied to both MSI and OLI, respectively. The pre-launch characterization of L8/OLI, 50-100% higher than its specification (Irons *et al*., 2012), shows that its SNR is much higher than the specification of S2/MSI (Vanhellemont *and* Ruddick, 2016). Therefore, since the resampling procedure applied to MSI data creates discrepancies in the spectral values of corresponding OLI pixels (especially over heterogeneous surfaces (Mandanici *and* Bitelli, 2016), x_{OLI} was assumed as x_{true} to prevent any instability of the SNR across the compared wavelengths.

2.6 FAI

Both MSI and OLI sensors contain a red, NIR, and SWIR channel all with very similar band-centers (Table 1) Therefore, a similar index in which both MSI and OLI can measure is the FAI. Because some bands between MSI and OLI vary in spatial resolution, the red band centered at 665 nm for MSI was resampled to match the vegetation red edge (VRE) and the shortwave infra-red (SWIR) 20 m spatial resolution required for calculations.

The FAI algorithm described by Hu (2009) is a simple ocean color index which introduced the detection of various floating algae and aquatic vegetation in the global oceans. Data comparison and model simulations showed that FAI is more advantageous than the traditional

NDVI or EVI because FAI is less sensitive to changes in observing conditions such as aerosols and solar viewing geometry (Hu, 2009). The FAI calculation, however, has not yet been included as a measure for the monitoring cyanobacterial blooms across turbid inland waters. Therefore, the FAI model was implemented in this research to provide an alternative approach to (1) quantify the extent and severity of an algal bloom over Utah Lake and (2) to explore the relationship between FAI and another index in which can subsequently estimate Chl-*a* concentrations and is not a shared index between the two sensors.

Algae floating on the water surface have higher reflectance in the NIR (800-900 nm) portion of the EMS than in other wavelengths (Hu, 2009). Hu (2009) determined that the difference between $\rho_{rc}(859)$ (NIR), and a baseline between 645 nm (red) and one of the short-wave infrared (1240 or 1640 nm) bands from MODIS can be used to detect floating algae, defined as:

$$FAI = \rho_{rc(NIR)} - \rho_{rc}'_{(NIR)} \quad (25)$$

$$\rho_{rc}'_{(NIR)} = \rho_{rc(RED)} + (\rho_{rc(SWIR)} - \rho_{rc(RED)})\,(\lambda_{(NIR)} - \lambda_{(RED)}) / (\lambda_{(SWIR)} - \lambda_{(RED)}), \quad (26)$$

where $\rho_{rc}'_{(NIR)}$ is the baseline reflectance in the NIR band derived from a linear interpolation between the red (665 nm) and SWIR (1610 nm) bands. This research utilized the FAI algorithm by applying it to all available, relatively cloud free imagery over the course of the 2016 Utah Lake bloom event for both MSI and OLI sensors. Additionally, performance sensitivity of the FAI algorithm between these sensors was evaluated through correlation. The underlying hypothesis predicted that the relationship of the FAI algorithm between any two cross-satellite sensors is robust enough to be extrapolated as long as it contains the required input bands.

2.7 NDCI & Chl-a

The abundance of Chl-*a*, a light harvesting pigment found in all oxygenic photosynthetic organisms, may be used as a proxy to assess the amount of algal biomass that is present in a water body (Ruiz-Verdu *et al*., 2008). Although extensive research has attempted to exploit the 620 nm absorption feature unique to the cyanobacterial pigment phycocyanin (PC) (Dekker, 1993; Schalles *and* Yacobi, 2000; Vincent *et al*., 2004; Simis *and* Gons, 2005; Mishra *et al*., 2009; Hunter *and* Tyler, 2010; Mishra *et al*., 2013; Mishra *et al*., 2014). MSI band configuration limits the direct measurements of cyanobacteria biomass due to the absence of a 620 nm band. However, NDCI, proposed by Mishra *and* Mishra (2011) is a standardized algal index that is used to predict Chl-*a* concentrations from remote sensing data in turbid productive waters. NDCI exploits the reflectance peak of Chl-*a* at 708 nm and the strong absorption feature in the red (665 nm) as:

$$NDCI \propto [R_{rs}(708) - R_{rs}(665)] / [R_{rs}(708) + R_{rs}(665)], (27)$$

where $R_{rs}(\lambda)$ is the remote sensing reflectance at that particular wavelength. In this study, however, modification to the NDCI formula to suite MSI band configuration (705 nm instead of 708 nm) was applied to all the Rayleigh corrected images following Mishra *and* Mishra (2011) as:

$$NDCI_{MSI} \propto [\rho_{rc}(705) - \rho_{rc}(665)] / [\rho_{rc}(705) + \rho_{rc}(665)] (28)$$

Rayleigh corrected reflectances ρ_{rc} were used rather than R_{rs} derived from the MAIN aerosol correction as the FAI algorithm originally developed by Hu (2009) called for ρ_{rc}, as ρ_{rc} are a popular metric in the ocean color community. Additionally, the FAI algorithm requires an SWIR band for calculation. Using the SWIR bands to determine ε will thus consume the SWIR bands rendering them unusable.

Mishra *and* Mishra (2011) showed that NDCI and Chl-*a* concentration have a strong relationship, producing an R^2 of 0.95 with a mean standard error of 2.49 mg m^{-3} ($p < 0.0001$) using ESA's Medium Resolution Imaging Spectrometer (MERIS) sensor. Following this logic, Chl-*a* concentrations were estimated from the resulting $NDCI_{MSI}$ images using the quadratic function (Mishra *and* Mishra, 2011):

$$\text{Chl-}a = 14.039 + 86.115\,(NDCI_{MSI}) + 194.325\,(NDCI_{MSI})^2, \quad (29)$$

Considering all cyanobacteria contain Chl-*a*, it must be noted that the application of this methodology is focused on the development of a phenological assessment tool for a known cyanobacteria bloom event, not to discern between toxic and non-toxic cyanobacteria species.

2.8 Cross calibration of MSI and OLI

Considering the absence of the band centered at 705 nm on the OLI sensor (Table 1), calculation of NDCI and subsequently Chl-*a* concentrations was not directly possible. The novel approach to compensate for the limitation of the OLI sensor, the relationship between processed MSI FAI and NDCI, denoted from here on as FAI_{MSI} and $NDCI_{MSI}$ respectively, was analyzed from a region of interest (ROI) (n = 30,052) within Utah Lake near the Powell Slough Waterfowl Management Area (PSWMA). The resulting regression equation between FAI_{MSI} and $NDCI_{MSI}$ was used to convert the OLI processed FAI images (FAI_{OLI}, independent variable) into NDCI images ($NDCI_{OLI}$, dependent variable). $NDCI_{OLI}$ were further processed for Chl-*a* (Chl-a_{OLI}) concentration determination following Equation (29). Resulting Chl-a_{OLI} products were then compared to Chl-a_{MSI} predictions for sensor dependency. Differences observed in the Chl-a_{OLI} estimates relative to Chl-a_{MSI} were quantified through a pixel-by-pixel percent error analysis (PEA) to derive a new correction coefficient matrix for the calibration of the OLI sensor to match Chl-a_{MSI} readings, considering MSI was the original sensor which contained the 705 nm band for NDCI calculation.

2.9 Cyanobacterial Cell Density (CCD)

Cyanobacteria detection in Utah Lake was performed by sampling crews conducted by the UDEQ that started on July 13th, 2016, after the bloom was reported on July 11th, 2016. After processing and analyzing these samples in the lab, results were posted along with sampling location information on the official website of UDEQ (http://deq.utah.gov/Pollutants/H/harmfulalgalblooms/bloom-2016/utah-lake-jordan-river/data.htm). However, lab analysis for cell count extraction requires tremendous effort and doing it on a regular basis by collecting field samples is not feasible from both economic and time perspectives. Additionally, water quality parameters collected during these field campaigns is in the form of limited point data, and often fails to deliver an accurate representation or magnitude of the bloom. Many satellite based studies used Chl-*a* concentration as a proxy for this purpose (Reinart *and* Kuster, 2006; Ahn *et al*., 2006; Zhao *et al*., 2010). In addition, previous studies based on field samples also revealed that peak Chl-*a* concentration coincided with peak PC (a proxy of cyanobacteria) concentration (Kanoshina *and* Leppanen, 2002; Mishra *et al*., 2009). Following this logic, CCD data from UDEQ sampling activities were correlated with Chl-*a* concentration derived from satellite data analysis, assuming all CCD measurements derived are from the known toxic-forming cyanobacteria species collected by UDEQ. The MSI image corresponding to July

15th, 2016 was used to correlate modeled Chl-*a* concentrations with *in-situ* CCD coinciding to the closest sampling dates (July 13th, 2016 – July 16th, 2016). Because of sun glint artifacts encountered from the satellite imagery during this time, only samples collected from the upper portion of the lake were used for correlation. A total of 12 cyanobacteria samples were considered and Chl-a_{MSI} concentrations extracted from those 12 pixels were used to establish a relationship with CCD. Unfortunately, this is all the data that was available from UDEQ.

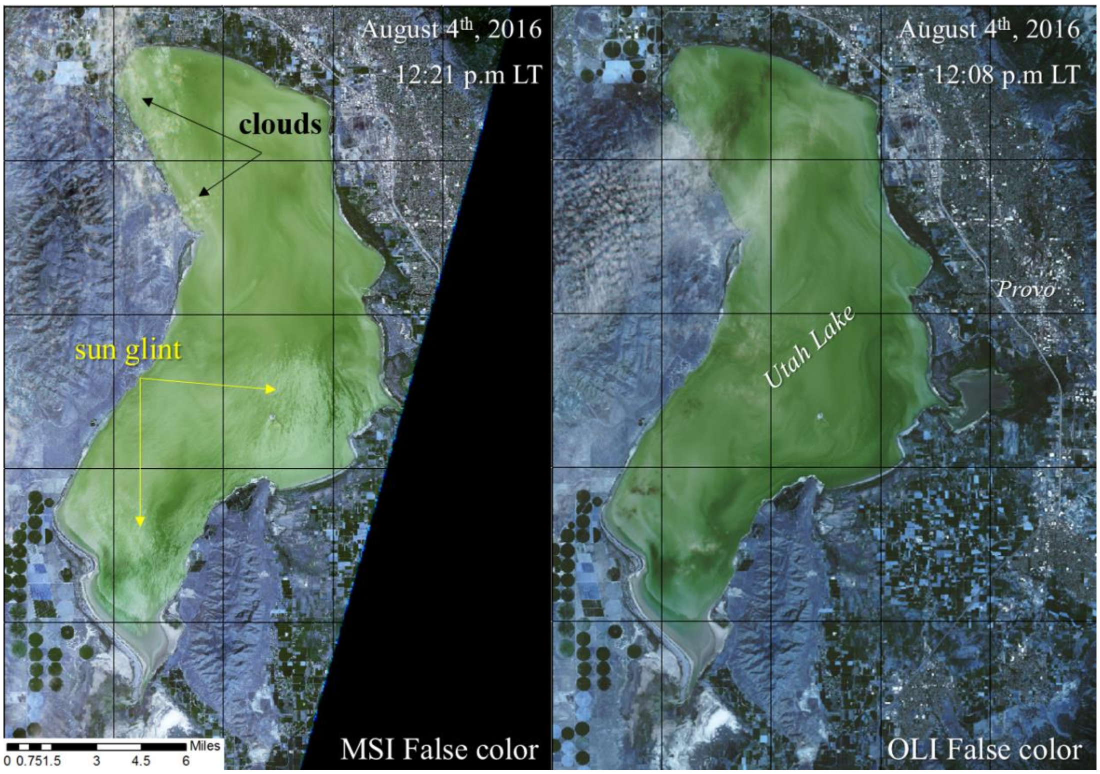

Figure 1. False color (RGB: BGB) ρTOA composites of Utah Lake captured by LS8 OLI (right) at 12:08pm and S2A MSI (left) at 12:21 pm local time during a coinciding overpass date on August 4th, 2016.

Table 1. Comparison of MSI and OLI input bands for applied models and corresponding band-centers and bandwidths.

Band ID	MSI band-center (nm)	MSI bandwidth (nm)	OLI band-center (nm)	OLI bandwidth (nm)	Applied Model
RED	665	30	655	30	FAI / NDCI
VRE 1	705	15	n/a	30	NDCI
VRE 2	865	20	865	30	FAI
SWIR 1	1610	90	1609	80	FAI

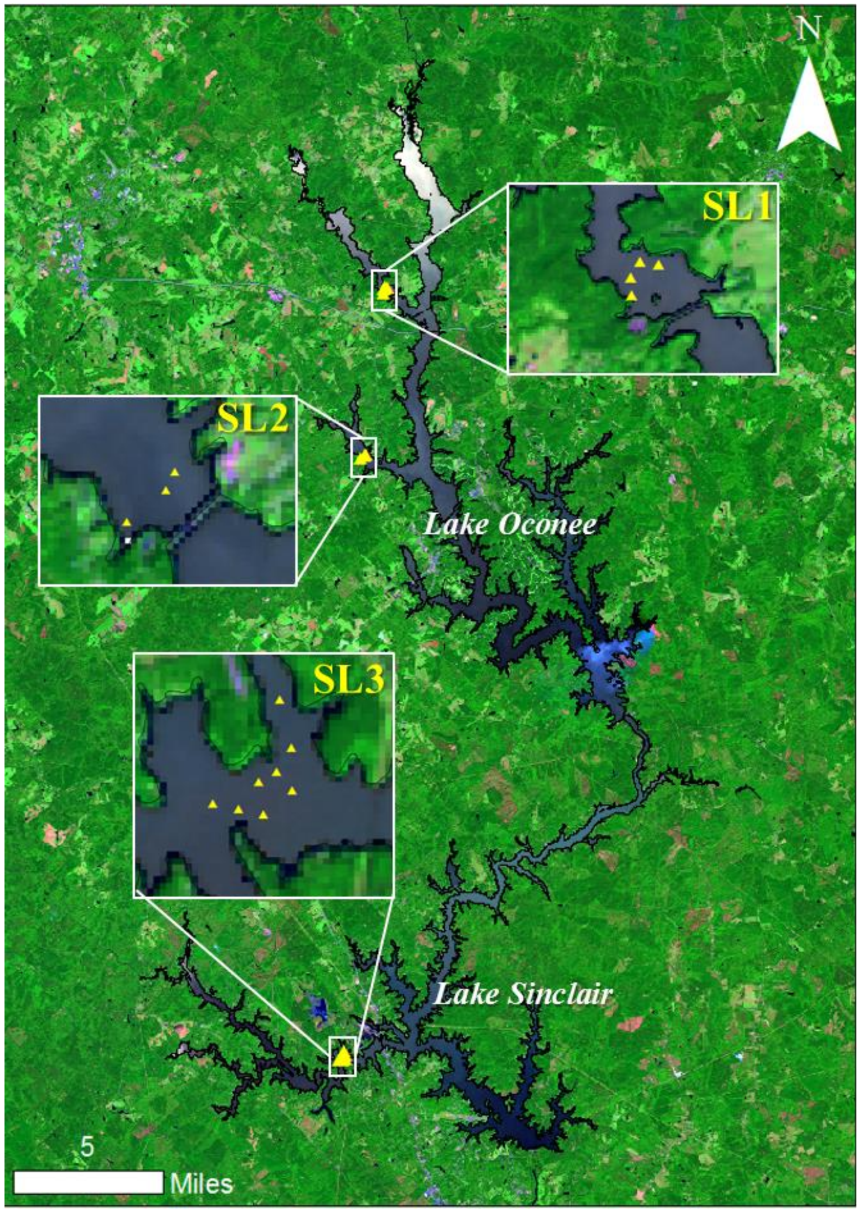

Figure 2. False color composite (RGB / OLI: 752) of Georgia's (USA) Lake Oconee and Lake Sinclair captured by LS8 OLI on October 22nd, 2014. Yellow tringles represent the three sampling locations (SL) conducted during the coinciding overpass of the satellite.

Table 2. BRIEF DESCRIPTION OF FOUR COMMONLY USED ATMOPSHERIC CORRECTIONS

Correction Method	Description	Source
Dark Object Subtraction (DOS)	*Dark object subtraction* searches each band for the darkest pixel value. Assuming that *dark objects* reflect no light, any value greater than zero must result from atmospheric scattering. The scattering is removed by *subtracting* this value from every pixel in the band.	(Chavez, 1988)
LS8 USGS Surface Reflectance Product (LS8-SRP)	*LS8-SRP* relies on the inversion of the relatively simple equation in the Lambertian case with no adjacency effects, that accounts for a simplified coupling of the absorption by atmospheric gases and scattering by molecules and aerosols as it is implemented in the 6SV radiative transfer code.	(Vermote, E. F., *et al.*, 1997b & Kotchenova, S. Y., *et al.*, 2006)
ACOLITE	*ACOLITE* is the first atmospheric correction procedure for LS8 specifically for the obtaining of water-leaving reflectances. The methodology addresses Rayleigh scattering and incorporates the short-wave infrared bands for aerosol mapping. This study incorporated the RV-SWIR (S, L) approach to also characterize aerosol type.	(Vanhellemont *and* Ruddick, 2014; 2015)
Fast Line-of-sight Atmospheric Analysis of Spectral Hypercubes (FLAASH)	In *FLAASH*, model simulations of the spectral radiance are performed for appropriate atmospheric and viewing conditions over a range of surface reflectance. The desired properties (reflectance, column water vapor, etc.) are derived from the spectral radiance at each image pixel using look-up tables that are generated from these simulations	(ENVI, 2009; Adler-Golden *et al.*, 1999)

CHAPTER 3

RESULTS AND DISCUSSION

3.1 UDEQ field campaign

UDEQ published historical water quality and CyanoHAB data for Utah Lake on their publicly available website (http://deq.utah.gov/) that shows increasing trends of cyanobacterial presence which reached up to an unprecedented level (36 million cells/mL) in July 2016 (Figure 3). Once the 2016 bloom was reported, UDEQ started frequent monitoring of the lake with weekly field sampling and results corresponding to each sampling location were posted on it's website (http://deq.utah.gov/Pollutants/H/harmfulalgalblooms/bloom-2016/utah-lake-jordan-river/index.htm) after analysis (Figures 3b-d). The severity of the bloom around the closure date of the lake (July, 14 -16) is evident in Figure (3b). Sampling locations around Utah Lake State Park and Lincoln Beach revealed the highest CCD exceeding 10 million cells/mL (Figure 3b). Even Jordan River, connecting to the lake from the northern side showed significantly high levels reaching 10 million cells/mL. By July 26th, reductions in cell counts were observed in the field samples analyzed by UDEQ and also visible in Figures 3(c-d) However, these maps were point-based analysis and could not reveal the full spatial extent of bloom distribution. On the other hand, the full extent of the bloom can be clearly observed in the false color composite satellite image derived from Landsat-7 (Figure 3e).

3.2 Satellite data – Utah Lake

S2A MSI and LS8 OLI shared a coinciding overpass date on August 4th, 2016 over Utah Lake, capturing a significantly large cyanoHAB spanning across the lake's entire surface area. With MSI overpass time at 18:21:55.985Z (~12:21 p.m local time) and OLI at 18:08:13.5692030Z (~12:08 p.m. local time), differences in cloud cover were observed between the two images. After masking for clouds and artifacts due to sun-glint for the MSI image, 57.1% of the pixels comprising the 368.5 square kilometer (km^2) lake was available for analysis in a multispectral feature space. Similarly, cloud cover affected only 18.2% of the lake pixels during the OLI overpass, leaving approximately 116 mi^2 for analysis. Finally, the two images were combined after resampling MSI from its native resolution (10m for RGB, 20m for NIR, 60 m for SWIR) to match OLI 30m spatial resolution, and any non-overlapping areas were eliminated. Remaining pixels covering approximately 124.8 km^2 (33%) of the lake area was available for the selection of an ROI which contained n = 30,052 pixels for band comparisons.

3.3 MAIN Performance – Utah Lake

Atmospherically corrected R_{rs} values obtained from the MAIN algorithm overall generated realistic, non-negative values across Utah Lake for both MSI and OLI sensors (Figure 4a-h). High R_{rs} values in the green bands [MSI (560 nm)/OLI (561 nm)] is most likely attributed to the reflectance properties of Chl-*a* pigments in the cells of cyanobacteria which have a reflectance maxima at ~575 nm and ~700 nm. Similarly, high intensities observed in the red bands [MSI (665 nm)/OLI (655 nm)] imply areas where suspended particulate matter (SPM) are the dominant influence (Nechad *et al*., 2010). The absence of a similar signal in MSI (665 nm)/OLI (655 nm) in the same areas where MSI (560 nm)/OLI (561 nm) is high further indicates the presence of Chl-*a* species which also have an absorption maximum at 665 nm (Mishra *and* Mishra, 2011). Additionally, MSI has a band centered at 705 nm (not shown), another reflectance maximum signature for the direct measurement of Chl-*a*. These observations highlight the capabilities of MSI for water quality monitoring in regards to algal biomass quantifications.

The utilization of two SWIR bands for an aerosol correction most noticeably allows the preservation of the NIR band(s) for R_{rs} computation (Figure 4d & 4h). While the NIR-based aerosol method's assumption of a zero water-leaving reflectance in optically complex waters leave the NIR bands unusable, the SWIR-based approach allows the NIR bands to be utilized in bio-optical models and other simple water quality band ratio analyses. It is important because the utility of the NIR bands in monitoring the quality of inland turbid productive waters has been demonstrated frequently in the last decade (Dall'Olmo *et al*., 2003; Gilerson *et al*., 2010; Mishra *et al*., 2013; Moses *et al*., 2012). It is also apparent that the OACs within Utah Lake have an influence on the water-leaving reflectance at MSI-864 nm / OLI-865 nm in some areas. This would lead to an over-estimation of aerosol contribution and result in negative water-leaving reflectances in those areas, generating unnecessary masked pixels (Dash *et al*., 2012; Vanhellemont *and* Ruddick, 2015). This observation supports the claim that an NIR-based aerosol correction would not be the most reliable option for productive inland waters for water quality purposes.

Distribution patterns of the water surface features for cloud-free pixels remains preserved across both sensors before (not shown) and after (Figure 4a-h) atmospheric correction. These results are not surprising as the linear correlations between the MSI and OLI sensors have been demonstrated by (Mandanici *and* Bitelli, 2016) and (Vuolo *et al*., 2016). However, ρTOA between the two sensors experienced significant errors in magnitude relative to each other (Table 3). Although positive linear correlations of the reflectance values exist across the comparable wavelengths before correction (Table 3, linear fit, before MAIN), the overall average signal received by MSI was found to be 54% lower than that retrieved by OLI (Figure 5a), with lower error in the blue/green and higher error in the red/NIR portion of the EMS (Table 3, MAPE, before MAIN). This is mainly attributed to the effect of the resampling procedure of MSI data to match OLI's 30 m resolution (Mandanici *and* Bitelli, 2016). After implementing the MAIN algorithm on either dataset, R_{rs} not only preserved positive linear correlations across all wavelengths for both sensors, but also tuned the reflectance magnitude closer to a 1:1 line (Table 3, linear fit after MAIN) and significantly ($p < 0.05$) reduced the band-by-band MAPE comparisons, with a minimum of 3.3 % between MSI (496)/OLI (483) ($R^2 = 0.86$) and a maximum of 15.4% between MSI (864)/OLI (865) ($R^2 = 0.80$).

Characterization of mean ρTOA, atmospherically corrected R_{rs}, Rayleigh and aerosol radiance are shown in Figure (5a-d). Since Rayleigh scattering is highly dependent on solar and viewing geometries and the location of the observation site within the scene (Dash *et al*., 2012), L_r values (Figure 5c) computed by the MAIN algorithm were in good agreement between MSI and OLI considering the coinciding overpass path on August 4th, 2016, a thirteen minute delay in image capture, and the nadir-viewing nature of the pushbroom sensors. Interestingly, although the mean ρTOA and R_{rs} signals retrieved by MSI are lower than that measured by OLI, radiance due to the multiple scattering of aerosols (L_{am}), on average, seemed to show more of a contribution in MSI than that measured by OLI. Though spectral shapes of L_{am} remained the same, the 90 nm and 180 nm bandwidths of the two SWIR channels of MSI would suggest a reduced signal-to-noise ratio in these wavelengths. The increased intensity of L_{am} by the MSI sensor could be explained by a change in atmospheric properties during the thirteen minute time difference between the coinciding overpass of both sensors.

Indeed, a higher percentage of clouds covered Utah Lake (46.3% cloud coverage) during the MSI overpass than the OLI overpass (only 18% of cloud coverage), suggesting an increase water vapor content, however, a study on the rate of aerosol and water vapor distribution across short spatial scales could not be found to support this hypothesis.

3.4 MAIN Validation – Lake Oconee / Sinclair

Confidence in the MAIN algorithm R_{rs} values for both MSI and OLI were derived from a dataset collected in the field on October 22nd, 2014 during a coinciding OLI overpass (Path: 18, Row: 37). During this time, S2A had not yet been launched, and *in-situ* spectroradiometer measurements could only be statistically compared to OLI derived R_{rs} from the MAIN algorithm. Collecting remote sensing data in the field relies on a time window which is defined to be short enough to reduce the effects of temporal variability in the in situ data, yet sufficiently large to allow for the greatest possibility of a match (Bailey *et al*., 2000; Bailey *and* Werdell, 2006). Fortunately, with prior knowledge regarding flight track time of the OLI sensor, fieldwork was completed within a 3 hour window. Figure (6) displays the spectral profiles of each sampling site collected by GER-1500 spectroradiometer at Lake Oconee / Sinclair (red solid line) with corresponding MAIN modeled R_{rs} values (black solid line). The performance of the MAIN algorithm relative to *in-situ* R_{rs} exhibited very similar spectral shapes and signal intensities across each sampling site, specifically sites 6, 7 and 10. Ultimately, the differences in spectral shapes at the other study sites is due to variability of the OACs in the water column. Relative comparisons between the two variables demonstrated the feasibility of the MAIN algorithm for a potentially operational method for reducing atmospheric noise over inland waters, with a MAPE of 8.7% for OLI (561nm) and a MAPE of 16.6% for OLI (655nm) compared to that of ACOLITE which resulted in a MAPE of 32.3% for OLI (561nm) and a MAPE of 23.6% for OLI (655nm). Interestingly, the USGS LS8-SRP product outperformed the MAIN algorithm only for OLI (655nm) with a MAPE of 11.1%, and the DOS method developed by Chavez (1988) out-competed both of these methods for OLI (655nm) with a resulting MAPE of only 2.4%. However, the performance of these two methods (LS8-SRP and DOS) for OLI (561nm) was nearly two- and three-fold worse than that of the MAIN algorithm. Performance evaluation through MAPE and *n*RMSE for each atmospheric correction used for the Lake Oconee / Sinclair in this study is displayed in Table (4), where bold numbers represent the lowest error generated from each atmospheric correction for each band. FLAASH on the other hand performed the worst, with a minimum MAPE greater than 90% in the blue band [OLI (483nm)], and therefore was excluded from further analysis.

Investigating further into the performance of each atmospheric correction relative to *in-situ* R_{rs} measurements, spectral shapes were analyzed visually and can be seen in Figure (7). Variability of *in-situ* R_{rs} intensities across each band can be seen throughout the dataset (black dashed lines). The ability of each atmospheric correction method (blue dashed lines) to match that variability and magnitude is the ultimate qualification for best performance. Spectral patterns resulting from ACOLITE relative to those collected *in-situ* show an overall similar behavior, however, the SWIR-based approach in this method seemed to have led to an underestimation of aerosol concentration across all wavelengths, as can be seen by the reduced magnitude of signal intensity (Figure 7c). This will ultimately lead to the underestimation of water quality parameters such as SPM or Chl-*a* concentrations at each site when incorporated into bio-optical models. These results are similar to those found by Bernardo *et al*., (2017).

Although LS8-SRP and DOS outperformed the MAIN algorithm for OLI (655nm), an important band in which SPM measurements are calculated (Nechad *et al*., 2010, Vanhellemont *and* Ruddick, 2014; Dogliotti *et al*., 2015) relative to statistical closeness (Table 4), the R_{rs} spectral shapes modeled by these two methods when compared to the spectral profiles generated the MAIN algorithm are obviously dissimilar (Figure 7b, d and e). For example, the R_{rs} maximum generated from the DOS method for OLI (561nm) was less than the R_{rs} minimum collected *in-situ* (Figure 7e). Similarly the R_{rs} minimum generated from the LS8-SRP method for OLI (865nm) was greater than the R_{rs} maximum collected *in-situ*. However, it is apparent that all R_{rs} values generated from the MAIN algorithm for OLI (483nm), OLI (655nm), and OLI (865nm) lie inside the range collected *in-situ*. Many studies involved in the remote sensing of lake water color rely on both simple and complex band-ratio algorithms for determining various water quality parameters (Pierson *and* Strömbeck, 2000; Härma *et al*., 2001; Östlund *et al*., 2001; Simis *et al*., 2005; Mishra *et al*., 2009). Therefore, it is necessary for all spectral bands to be as consistent as possible relative to those collected *in-situ* using a single atmospheric correction method.

Minor differences in the spectra of each atmospheric correction can be seen looking at two different study sites in which each atmospheric correction method performed best relative to the other sites (Figure 8) Once again the entire spectral shape generated from the MAIN algorithm seems to match most appropriately to that collected *in-situ* for both sites. The consistent irregular spectral shape of the DOS method from OLI (483nm) to OLI (655nm), however more accurate than in the OLI (655nm) calculated by the MAIN algorithm, would lead to false estimations in simple green/blue and green/red band ratio-algorithms. Therefore, one should use caution when using these simple correction methods and carefully consider the atmospheric properties being quantified.

3.5 FAI, NDCI, Chl-*a* & CCD

The FAI algorithms appears to be sensor independent after a strong positive linear correlation ($R^2 = 0.898$, $p < 0.001$, $n = 30{,}052$) was observed between both FAI_{MSI} and FAI_{OLI} within the ROI (Figure 9a) on the August 4th, 2016 image (Figure 9b). The MSI image on August 4th, 2016 over Utah Lake was processed for NDCI ($NDCI_{MSI}$) and subsequent Chl-*a* concentrations. To assess whether the OLI sensor can accurately match Chl-*a* estimates retrieved from MSI even though it lacks the necessary band centered at 705 nm, the relationship between FAI_{MSI} and $NDCI_{MSI}$ was examined. A significant positive linear relationship ($R^2 = 0.935$, $p < 0.001$) was found between FAI_{MSI} and $NDCI_{MSI}$ based on the $n = 30{,}052$ pixels derived from the sampling ROI location (Figure 9c). The resulting linear regression extracted between the two variables was used to process all FAI_{OLI} images into $NDCI_{OLI}$.

$$NDCI_{OLI} = 3.4374 * FAI_{OLI} + 0.212, \quad (30)$$

where $NDCI_{OLI}$ was further processed to estimate Chl-*a* concentration (Chl-a_{OLI}) once again following the logic of Mishra and Mishra (2011), modified for the OLI sensor:

$$\text{Chl-}a_{OLI} = 14.039 + 86.115\,(NDCI_{OLI}) + 194.325\,(NDCI_{OLI})^2, \quad (31)$$

This not only reveals new possibilities with unexplored OLI capabilities, but also assists in increased temporal quantification of bloom coverage when coupled with the MSI sensor.

Values of Chl-*a* estimates after NDCI calculation were extracted from the same ROI (n = 30,052) near the PSWMA (Figure 9a) for the coinciding overpass date (August 4th, 2016) for both OLI and MSI (Figure 9d). Resulting Chl-a_{OLI} estimations when compared with Chl-a_{MSI} during validation showed a positive correlation (R^2 = 0.883), however, underestimations of Chl-a_{OLI} concentrations were also observed. This is in part due to the signal to noise ratio (SNR) loss experienced by MSI after resampling from 20 to 30 meters to match OLI's spatial resolution (Vanhellemont and Ruddick, 2016) and difference in cross-sensor bandwidths. Nonetheless, the objective here was to match Chl-a_{OLI} estimates as close to that being predicted by MSI (Chl-a_{SMSI}), even after a decrease (20m to 30m) in MSI spatial resolution by resampling. Therefore, PEA was performed on the original Chl-a_{OLI} estimates. This was accomplished by determining the percent error (PE) between each Chl-a_{OLI} and associated Chl-a_{MSI} pixel in which the resulting PE values are then added back to the original Chl-a_{OLI} pixel estimates:

$$\text{Chl-}a_{OLI\_CAL} = \text{Chl-}a_{OLI} + \text{Chl-}a_{MSI}\,(1 - (\text{Chl-}a_{OLI} / \text{Chl-}a_{MSI}))\quad(32)$$

where Chl-a_{OLI_CAL} is the calibrated Chl-*a* concentration estimation after PEA. The relationship between the August 4th Chl-a_{MSI} and the calibrated Chl-a_{OLI_CAL} processed images (R^2=0.98) seem to explain the concentration differences observed between the two sensors prior PEA as a result of the SNR loss experienced by MSI after resampling (Figure 10, before PEA). A significant improvement was observed after compensating the error which modified the slope (~1) and bias (0.3) (Fig. 10, after PEA).

The PEA method increased the overall predictions to the original Chl-a_{OLI} estimation, as expected, in all pixels to match readings closer to Chl-a_{MSI}. Chl-a_{OLI_CAL} was then regressed against the original Chl-a_{OLI} image to derive a linear equation ($R^2 = 0.94$) that can be applied on the other OLI images comprising the time series from June to August:

$$\text{Chl-}a_{OLI}^* = 1.5251 * \text{Chl-}a_{OLI} – 5.4534 \quad (33)$$

where Chl-a_{OLI}* is the corrected and final Chl-*a* concentration determination algorithm (Fig. 10, after PEA), which added one more step in estimating Chl-*a* concentrations after first being derived from $NDCI_{OLI}$.

Point-based maps and analysis conducted by UDEQ across the July 2016 bloom event could not reveal the full extent of the bloom coverage (Figures 3b-d). Therefore, calibration of Chl-a_{MSI} with UDEQ CCD field sampling data (n = 12) was accomplished through a linear regression ($R^2 = 0.62$; n = 12; $p < 0.05$):

$$CCD_{SAT} \text{ (cells / mL)} = 4{,}989.5 \text{ (Chl-}a_{SAT}\text{)} – 131{,}742 \quad (34)$$

where SAT is the either MSI or OLI_CAL. This relationship (Equation 34) was further used to create spatio-temporal maps of CCD over the entire lake. Time series composites of final RGB, FAI, Chl-*a* and CCD products containing all available imagery dates over the summer 2016 bloom event are displayed in Figures 11 and 12 from both MSI and OLI sensors respectively.

3.6 Time series composites

The time series composites of FAI maps revealed positive values (> 0.03) in the month of July, 2016 indicating a bloom condition in the lake (Figure 11, row 2). Hu (2009) showed the potential of FAI to isolate the areas affected by floating algae using both MODIS and Landsat ETM+ satellite sensors. However, both being relatively new operational satellite sensors, neither MSI nor OLI data have ever been used to incorporate this index by a means to quantify a cyanobacterial bloom. Spatio-temporal analysis of the Chl-a_{MSI} maps revealed similar patterns for the bloom onset (first week of July), peak level (mid-July), and then decay of the bloom (August) as reported by UDEQ in their official website. A significant high level of Chl-*a* concentration can be clearly observed on July 15th, July 22nd, and even on August 4th spatial maps (Figure 11, row 3). Spatio-temporal maps of $\mathrm{CCD}_{\mathrm{MSI}}$ showed a somewhat faint sign of cyanobacteria in the middle of the lake before July 2016 (Figure 11, row 4). It should be noted that the CCD model (Equation 34) produced a bias of 131,742 cells/ml which indicated that the CCD model may produce higher error for low cell count areas. More field data from known CyanoHAB events are required to tune and validate this model for a broad CCD range. However, Provo Bay, wedged between the central-eastern coasts of the lake, showed measurable signs of cyanobacteria cells even in prior months. This could be associated with a considerable amount of sewage input as this area is very close to urban communities and waste water treatment plants. According to the Utah division of water quality, about 80% of the algal bloom causing phosphorous comes from effluent discharges by wastewater treatment plants. Apart from Provo Bay, a small indication of cyanobacteria growth was observed at the start of July (July 2nd, 2016) in the southernmost part of the lake which significantly increased in mid-July (July 15th and July 22nd, 2016) and covered almost the entire lake as observed from the time series analysis of spatial maps (Figure 11). The cell count was significantly high on July 15th, 2016 which corroborated with the results of field sampling reported by UDEQ (Figs. 3b-d and Fig. 11). However, the MSI image on July 15th, 2016 was affected by sun glint near the southeastern portion of the lake and could not show the full extent of the bloom. Cell count numbers reduced as the day progressed and only some areas near the southeastern shoreline of the lake indicated lower level of cell density on August 24th, 2016 and can be seen on the map (Figure 11).

Additional analysis of the OLI derived spatio-temporal maps of FAI, Chl-*a*, and CCD filled the gaps between MSI image dates (Figure 12). The OLI spatial maps produced starting from June 1st, 2016 through August 20th, 2016 followed a similar pattern (start of bloom on July 2nd, peak on July 19th, and lowest level on August 20th, 2016) to that of the MSI derived spatio- temporal maps (Figure 12). This continuity of a pattern validated that the two sensors can effectively be coupled in future studies for low cost continuous monitoring of algal blooms at increased temporal resolution.

3.7 Time series analysis

Mean values of Chl-*a* and CCD from each cloud and sun-glint free pixel corresponding to each date from both MSI and OLI sensors were plotted across the July 2016 bloom event timeline (Figure 13). Time series analysis of mean Chl-*a* and CCD clearly revealed the start-peak-decay of the bloom. Coupling of the two sensors provided a complete time series starting from June to August. Temporal patterns shown in Figure (13) included data from both MSI (total 12 images: June 12th , July 2nd, July 15th, July 22nd, August 4th, and August 24th) and OLI sensor (June 1st, June 12th, July 3rd, July 19th, August 4th, and August 20th) which together showed similar a trend of the bloom as reported by UDEQ in their daily updates related to the 2016 CyanoHAB.

A small increase in mean Chl-*a* concentration was observed on July 2^{nd} (mean Chl-*a*: 14.59 ug/L) from June 17^{th} (mean Chl-*a*: 8.84 ug/L), which significantly increased on July 15^{th} (mean Chl-*a*: 36.15 ug/L), and reached a maximum level on July 19^{th}, 2016 (mean Chl-*a*: 46.44 ug/L) (Figure 13). After July 19^{th}, Chl-*a* concentration reduced gradually and reached a similar level on July 3^{rd}, 2016 (mean Chl-*a*: 18.09 ug/L) and on August 24^{th}, 2016 (mean Chl-*a*: 18.01). A similar trend was found in CCD which showed significant jump in mean cell count on July 15^{th} (mean cell count: 108,176 cells/mL) from July 3^{rd}, 2016 (mean cell count: 9,163 cells/mL) and started reducing in following dates that reached a similar level compared to that of July 3^{rd} and on August 24^{th}, 2016 (mean cell count: 9,145 cells/mL) (Figure 13). These results not only validated the range and pattern shown using field sample data analyzed and published by UDEQ, but also reveals how fast a bloom can grow if the environmental conditions are favorable. These results demonstrate that satellite–based monitoring methods can be a great tool for lake resource managements and state agencies for regular monitoring and will reduce the budget cost for monitoring and predicting CyanoHABs in large lakes.

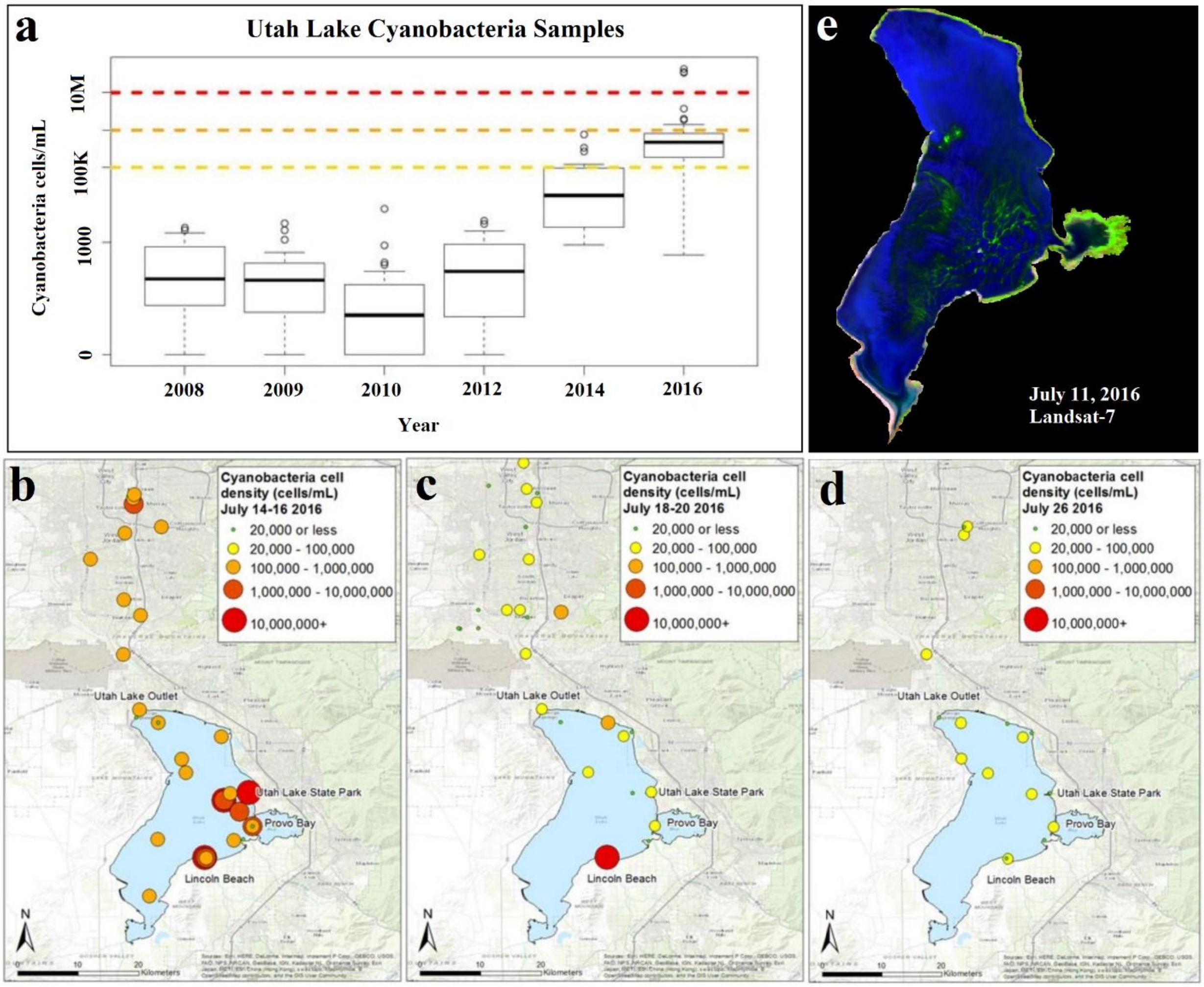

Figure 3. Historical comparison of cyanobacteria cell count in Utah Lake. Box plot of cyanobacterial cell density of Utah Lake from 2008 to 2016 measured by UDEQ, (a). The dashed yellow line is a warning threshold and the dashed red line represents lake closure threshold. Dates and sampling locations for cyanobacterial cell density during the July 2016 bloom (b-d). The floating algae was also captured by Landsat-7 image (RGB=5,4,2) and shown in green color (e). (Note: All images corresponding to field sampling results (a-d) were obtained from UDEQ).

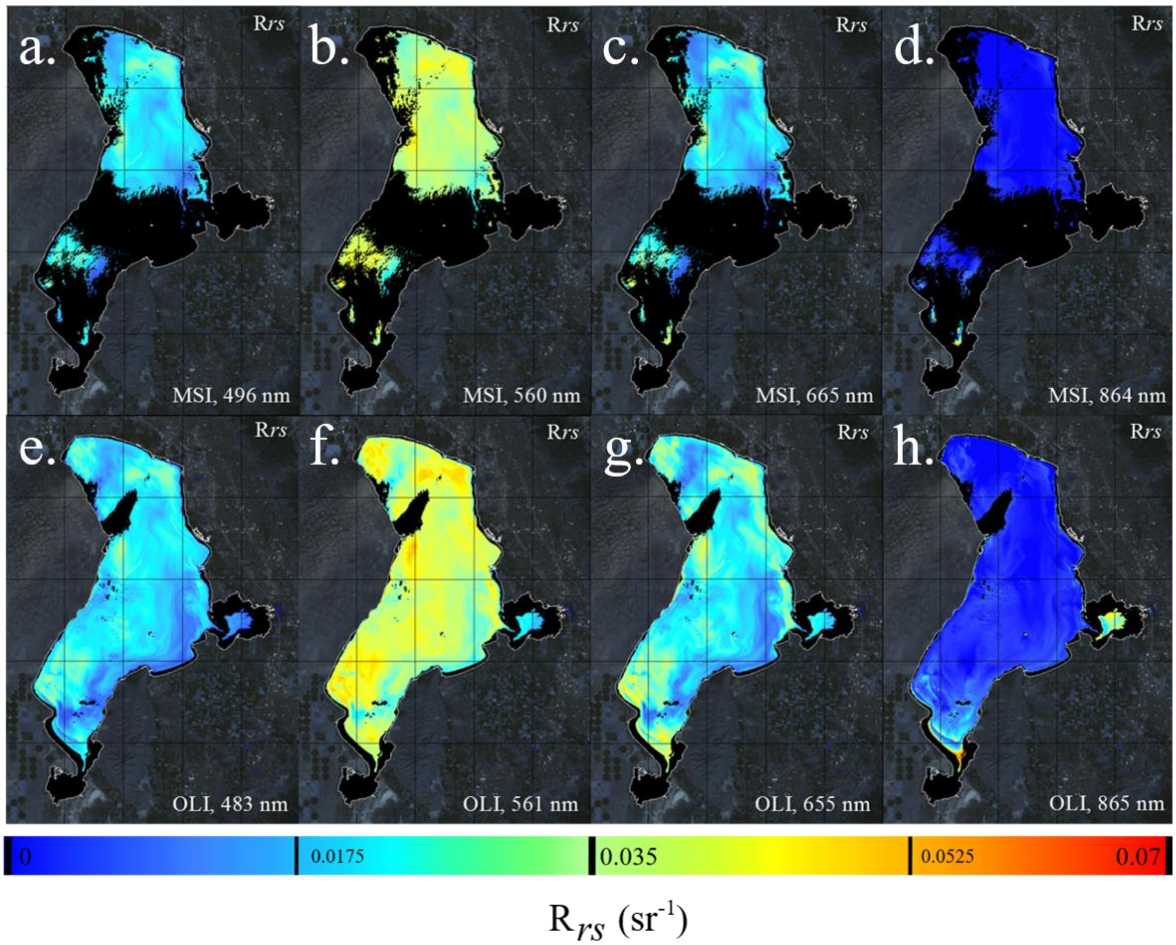

Figure 4. Pseudocolor distribution maps of R_{rs} over Utah Lake derived from MSI (top) and OLI (bottom) across all comparable wavelengths (a-h). Cloud masking and sun-glint removal is represented by black pixel regions

Table 3. Linear relationship (R^2) and mean absolute percent error (MAPE) between MSI and OLI band before and after MAIN atmospheric correction

	Before MAIN Correction			After MAIN Correction		
Band(λ)	**Linear Fit (y = mx + b)**	**R^2**	**MAPE (%)**	**Linear Fit**	**R^2**	**MAPE**
[MSI (496), OLI (483)]	$MSI_{TOA} = 0.956 \times OLI_{TOA} + 0.103$	0.86	45.82	$MSI_{Rrs} = 0.966 \times OLI_{Rrs} + 0.00014$	0.86	3.33
[MSI (560), OLI (561)]	$MSI_{TOA} = 0.824 \times OLI_{TOA} + 0.062$	0.88	42.08	$MSI_{Rrs} = 0.785 \times OLI_{Rrs} + 0.00591$	0.87	10.41
[MSI (665), OLI (655)]	$MSI_{TOA} = 0.832 \times OLI_{TOA} + 0.081$	0.92	54.94	$MSI_{Rrs} = 0.802 \times OLI_{Rrs} + 0.00268$	0.91	15.15
[MSI (864), OLI (865)]	$MSI_{TOA} = 0.730 \times OLI_{TOA} + 0.074$	0.72	73.73	$MSI_{Rrs} = 0.823 \times OLI_{Rrs} + 0.00102$	0.80	15.38

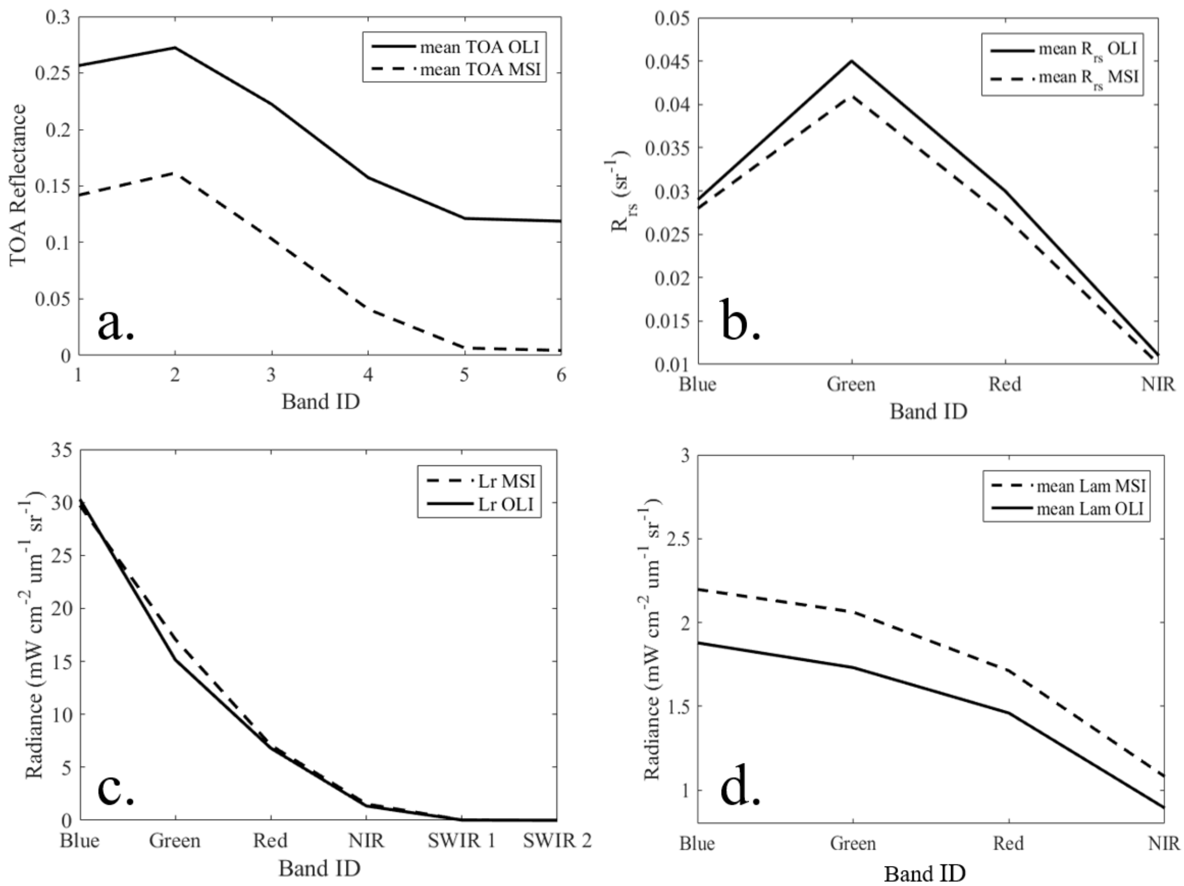

Figure 5. Spectra comparisons of mean ρTOA (a), R_{rs} (b), L_r (c), and L_{am} (d) (n = 30,200) between the coinciding overpass of OLI (black solid line) and MSI (black dashed line) on August 4th, 2016 over Utah Lake.

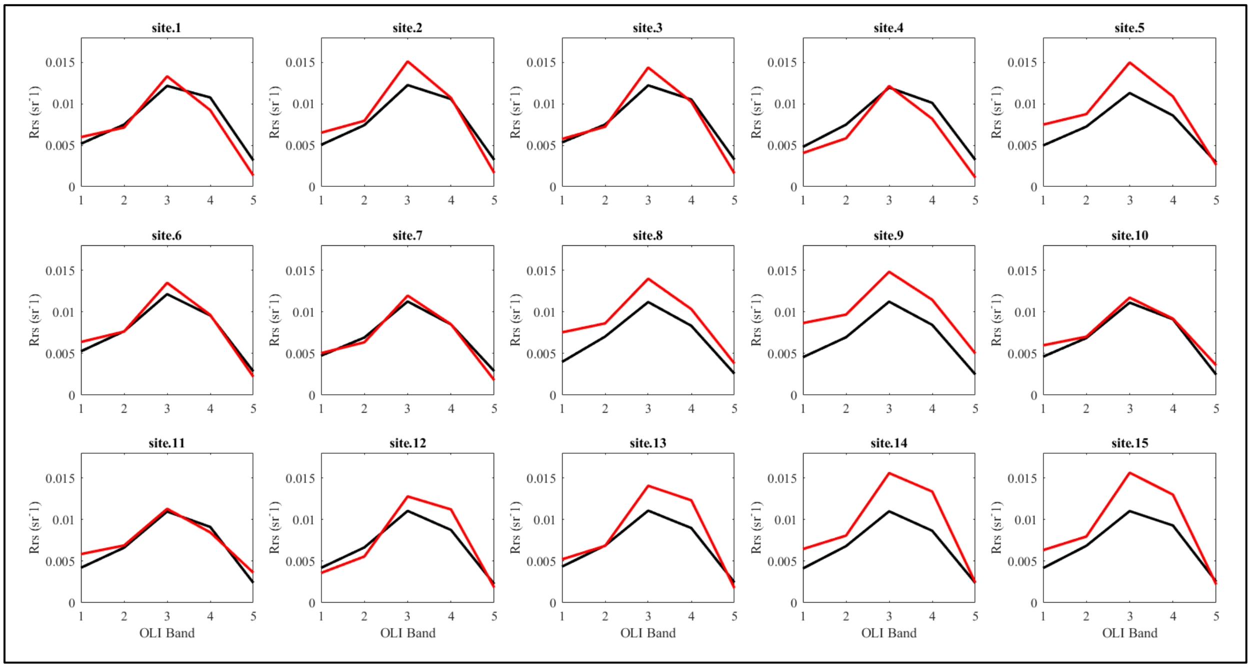

Figure 6. Spectral profiles of each SL site collected by GER-1500 hyperspectral spectroradiometer on October 22, 2014 (red) and corresponding R_{rs} estimates derived from atmospherically corrected (MAIN) OLI bands 1-5 (443, 483, 561, and 655 nm) (black).

Table 4. Band-by-band comparison through MAPE and Normalized Root Mean Square Error (*n*RMSE) analysis (%) between *in-situ* R_{rs} and each atmospheric correction method for the OLI image over Lake Oconee / Sinclair on October 22nd, 2014

Correction Method	***n*RMSE (%)**	**MAPE (%)**
ρTOA		
[OLI (483nm)]	609.1	1146.9
[OLI (561nm)]	413.6	430.9
[OLI (655nm)]	233.2	404.0
[OLI (865nm)]	109.1	1134.4
MAIN		
[OLI (483nm)]	36.4	**4.8**
[OLI (561nm)]	**27.1**	**8.7**
[OLI (655nm)]	55	16.6
[OLI (865nm)]	**35.1**	135.8
ACOLITE		
[OLI (483nm)]	60.3	43.4
[OLI (561nm)]	85.6	32.3
[OLI (655nm)]	97.9	23.6
[OLI (865nm)]	50.4	**54.8**
OLI-SRP		
[OLI (483nm)]	**31.4**	14.0
[OLI (561nm)]	54.5	19.1
[OLI (655nm)]	**30.7**	11.1
[OLI (865nm)]	73.6	292.9
DOS		
[OLI (483nm)]	28.5	7.4
[OLI (561nm)]	79.8	25.4
[OLI (655nm)]	26.9	**2.4**
[OLI (865nm)]	70	281.1

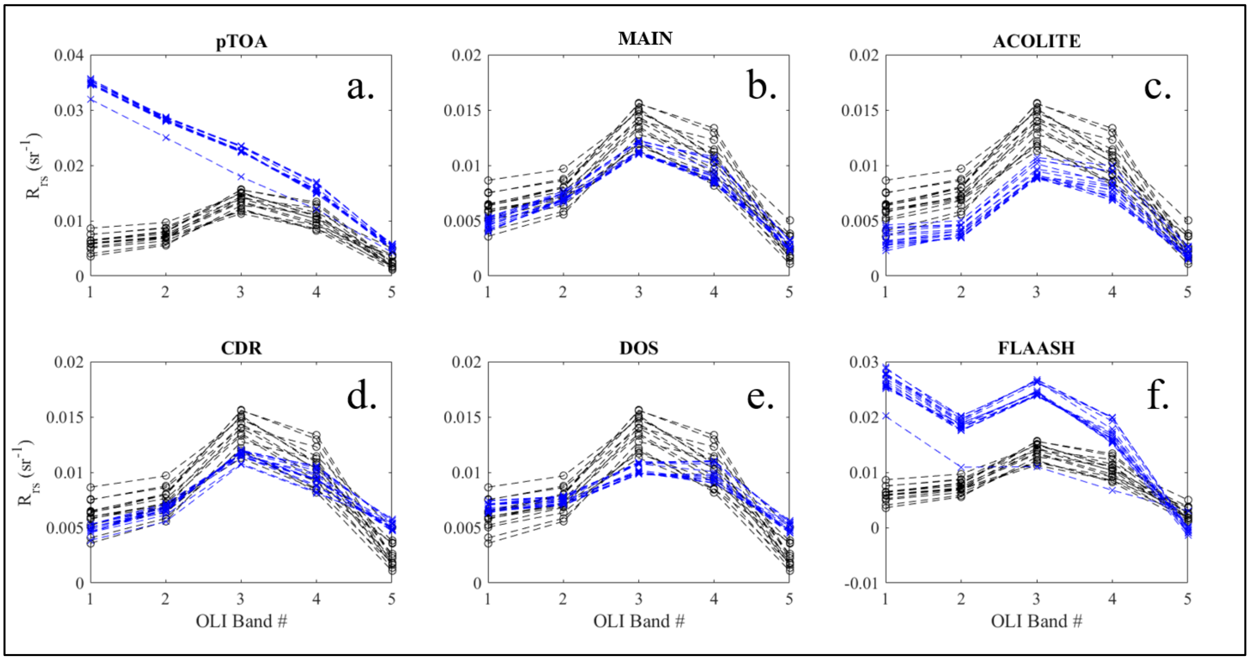

Figure 7. R_{rs} spectra of 15 study sites collected on October 22nd, 2014 at Lake Oconee / Sinclair (dashed black line) and corresponding spectra from each atmospheric correction method (dashed blue line).

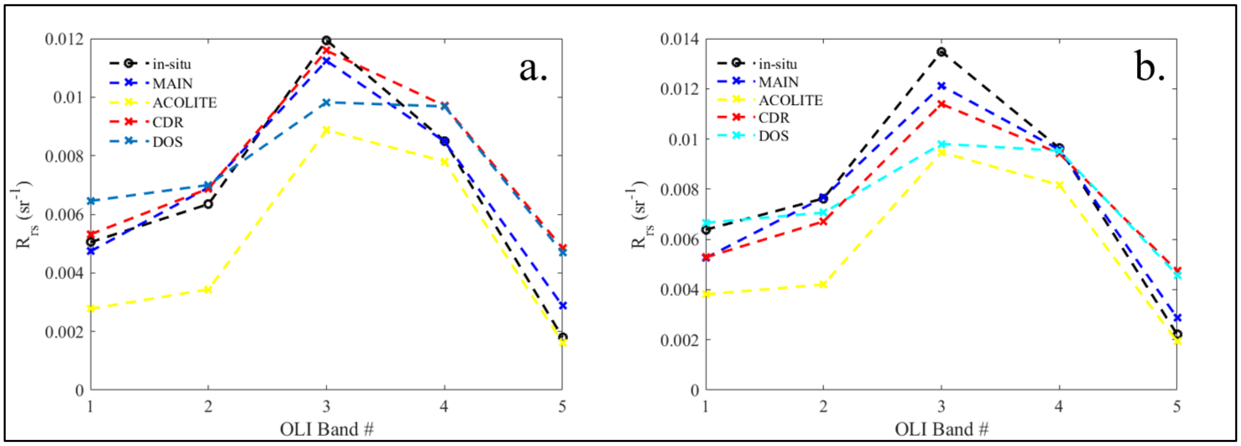

Figure 8. Spectral profiles from two different study sites on Lake Oconee / Sinclair (SS: 6, SL: 2 / SS: 10, SL: 3) after applying all atmospheric corrections excluding FLAASH.

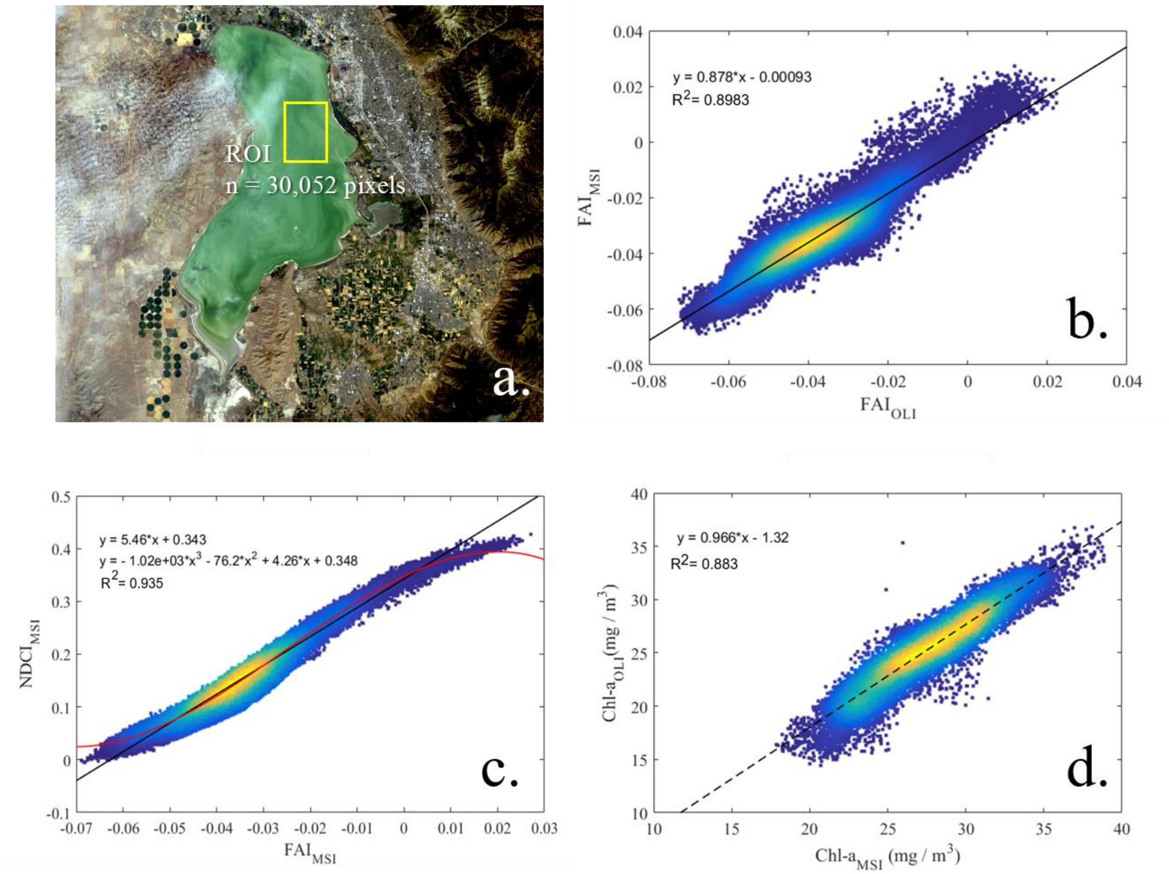

Figure 9. (a) OLI RGB composite on August 4th, 2016 showing sampling ROI (n = 30,052 pixels) near the PSWMA. (b) Density scatter plot between FAI_{MSI} and FAI_{OLI} layers. (c) Regression between $NDCI_{MSI}$ and FAI_{MSI} for $NDCI_{OLI}$ determination. (d) Relationship between Chl-a_{OLI} and Chl-a_{MSI} (before PEA).

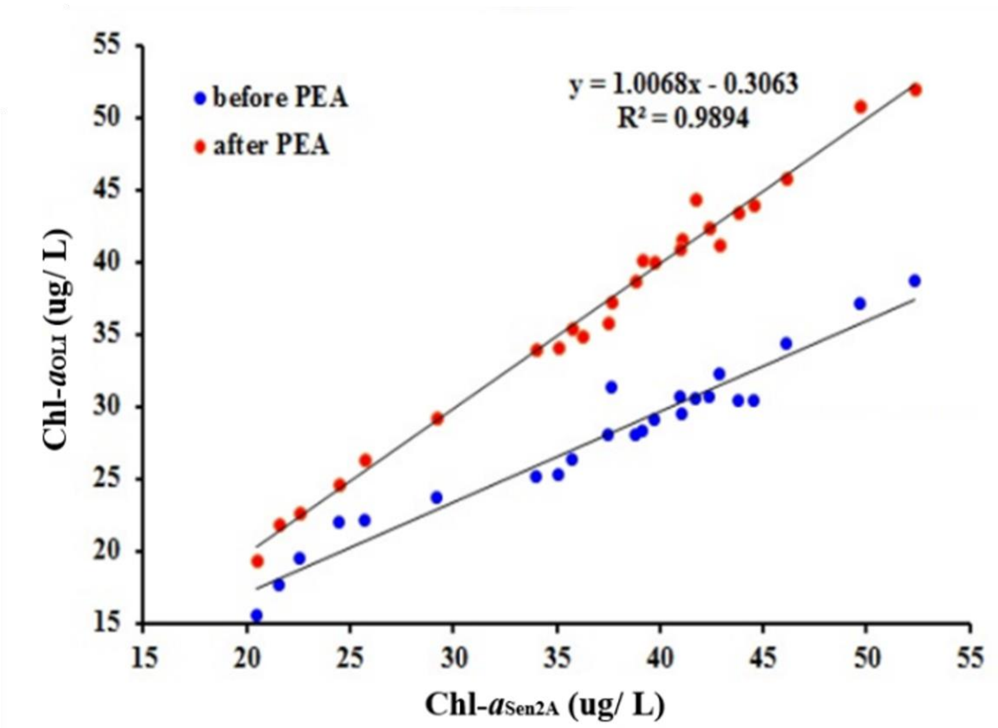

Figure 10. Relationship between August 4th, 2016 Chl-a$_{OLI}$ and Chl-a_{MSI} before and after PEA correction. Overall increase in Chl-a$_{OLI}$ signal after PEA compensates for the differences observed caused from the SNR loss when resampling MSI from 20 to 30 m.

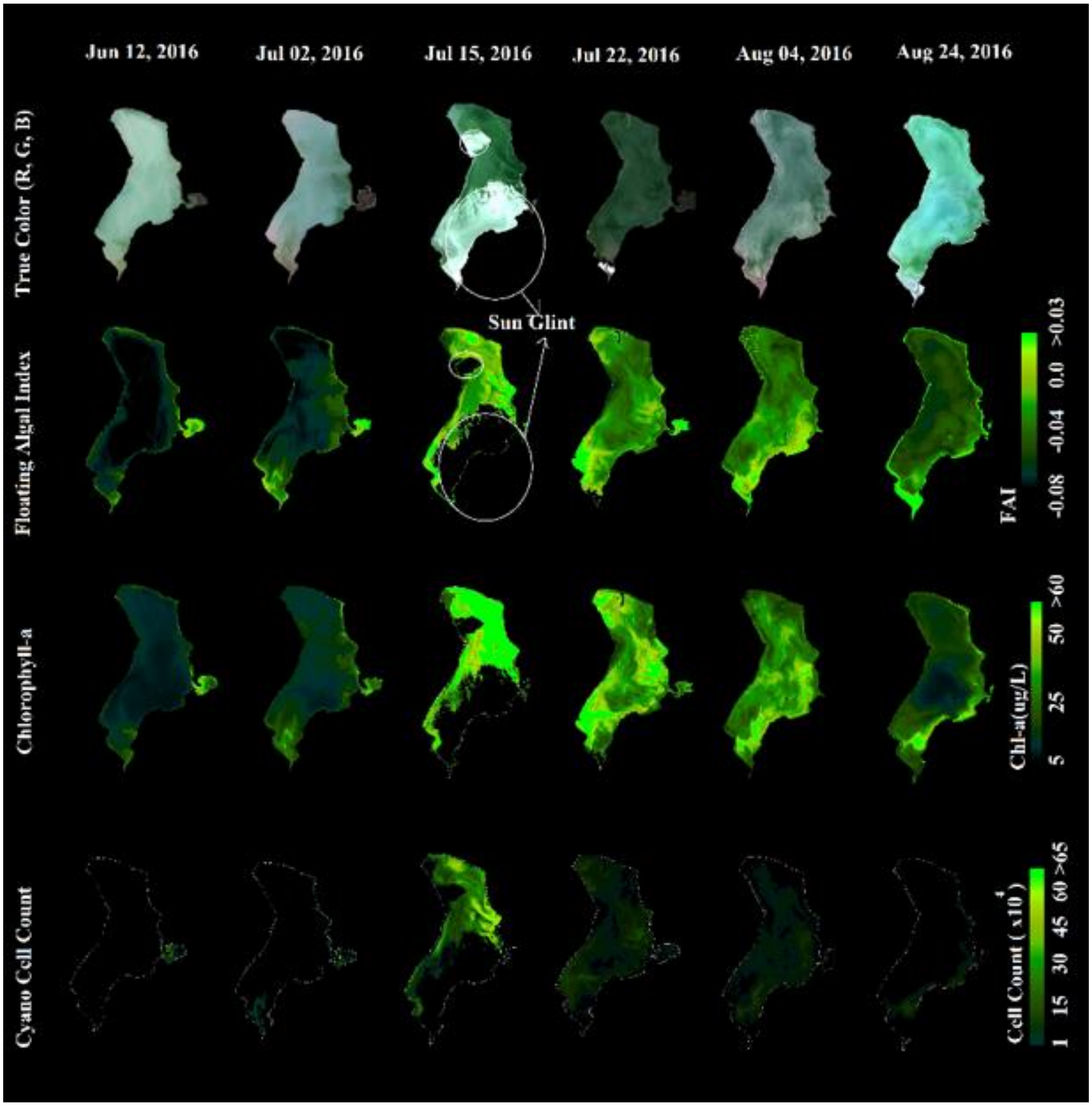

Figure 11. Rayleigh corrected, MSI derived spatio-temporal patterns of FAI, Chl-*a*, and CCD. True color images (RGB: 3,2,1) corresponding to each date are also included to compare the patterns in variability. Sun glint affected area are marked by open white circle, indicated by arrows and not included in the analysis.

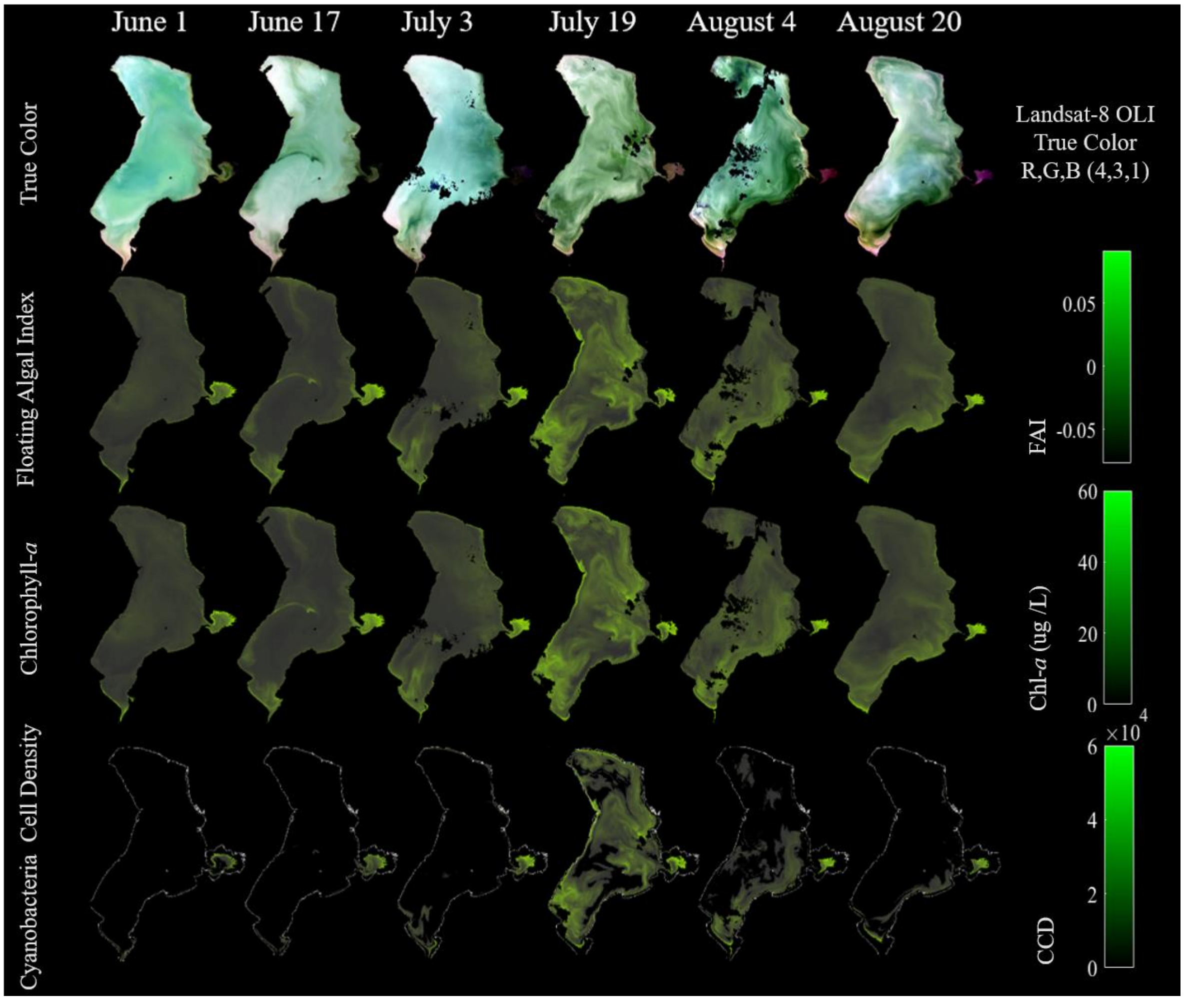

Figure 12. Rayleigh corrected LS8 OLI derived spatio-temporal patterns of FAI, Chl-*a*, CCD from June to August 2016. Black zones within the FAI and Chl-a images (July 3rd – August 4th) are a result of cloud masking during the pre-processing phase. Black zones within the CCD time series products were below the bias threshold of 131,742 (cell/ml) for the CCD model (Equation 34).

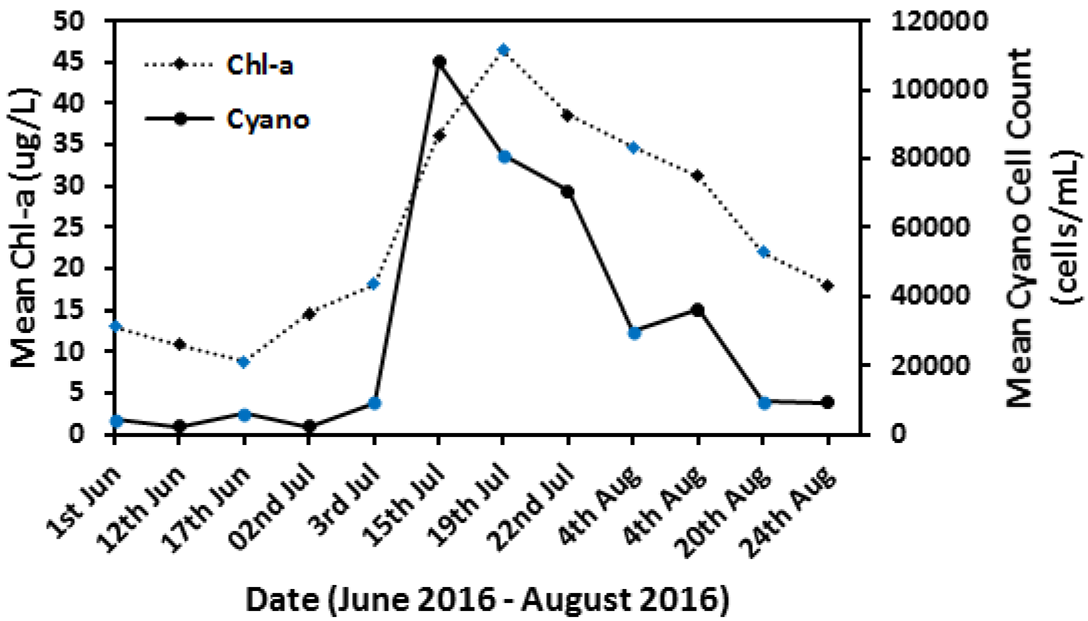

Figure 13. Time series values of Chl-*a* and CCD for all cloud free images incorporated in analysis. Both Sen2A and OLI derived concentration and cell density are included (MSI data points are marked in black colors and OLI data points are marked in blue colors).

CHAPTER 4

CONCLUSION

Effective quantification and phenological analysis of a massive CyanoHAB in Utah Lake using two operational satellite sensors was successfully achieved in this study. The efficacy of the MAIN algorithm when coupling LS8 OLI and S2A MSI sensors served as a viable alternative to derive accurate ρ_{rc}, ρ_w, and R_{rs} values for water quality bio-physical models than other commonly used atmospheric corrections. Additionally, cross-sensor calibration of NDCI from FAI provided a novel alternative way to use the OLI sensor for extracting NDCI and consequently estimating of Chl-*a* values without the presence of one of the two specific bands (705 nm) required for the computation.

Because of the overall conservation of spectral shape and the consistent low error associated between *in-situ* and the MAIN derived R_{rs} values relative to the performance of the other atmospheric corrections analyzed in this study, the MAIN algorithm should be considered for reference in future studies intending to derive OACs from inland water bodies for water quality purposes. For example, ESA's BEAM application is an open-source toolbox and development platform for viewing, analyzing and processing of remote sensing raster data. Originally developed to facilitate the utilization of image data from Envisat's optical instruments, BEAM now supports a growing number of other satellite instruments including the Sentinel and Landsat constellation. The accuracy of the retrievals acquired by comparisons with concurrent *in-situ* ground measurements was published in full detail elsewhere. For the remote sensing reflectance product when using BEAM, a mean absolute percentage error (MAPE) of 18% was derived within the spectral range 412.5–708.75 nm (Schroeder *et al*., 2007) while the accuracy resulting from the MAIN algorithm resulted with a MAPE of 10% in the spectral range from 443 – 655 nm.

Unlike the other atmospheric corrections tested (ACOLITE, DOS, LS8-SRP and FLAASH), the MAIN algorithm requires some user-input parameters for R_{rs} calculation such as site elevation and ozone concentration (in DU) of which can be conveniently retrieved from Google Earth and NASA's Ozone Over Your Head online application, respectively. Additionally, the MAIN algorithm generates maps of aerosol distribution (L_{am}) for each band to understand aerosol variability and spatial distribution over inland waters. Finally, the MAIN algorithm relived the need to perform any vicarious calibration often required by other ocean color platforms to empirically match the signal received by the satellite with ground radiometric measurements.

Cross-sensor comparisons between MSI and OLI R_{rs} values derived from the MAIN algorithm have resulted in significant relationships across all comparable bands, with high correlation coefficients as well as similar intensity readings. Of course, the overall accuracy of the estimated R_{rs} from MAIN processed MSI and OLI images for Utah Lake would improve with frequent, routine *in-situ* sampling consisting of both water surface radiometric measurements and atmospheric properties (ozone, aerosols) in a more systematic manner to fully understand the relationships between R_{rs} and the OACs in the water column. This would allow the formation of a much larger dataset to gain the confidence in the quantification of future water quality parameters.

Resulting CCD estimations in Utah Lake were a preliminary, novel way to quantify the cyanobacteria biomass using *in-situ* CCD measurement derived from UDEQ and Chl-*a* concentrations derived from satellite product. Considering the range of CCD during field sampling campaigns, the CCD model derived from MSI and OLI would not be able to detect lower concentrations of cyanobacteria biomass even though cyanobacteria may be present. This was partly due to the small sample size (n = 12) as clouds interfered with the lower portion of the lake and those samples collected by UDEQ had to be masked out to prevent unrealistic values. As the CCD model was calibrated with a Chl-*a* detection model and not a PC model, this method is only suitable for known cyanobacterial bloom assessments. Running the same model on a random inland water body to for the detection only of cyanobacteria without any local knowledge would not provide a reliable conclusion about whether the positive readings are from cyanobacteria or from another photosynthetic species containing chlorophyll.

Currently, there is no rapid, large scale operational tool readily available for monitoring this phenomenon other than through the use of satellite based remote sensing. Phenological assessment maps generated by the proposed methodology is a significant first step in providing a visual and quantifiable approach to understand the seasonal variability of a particular water body of interest. Additionally, time series analysis clearly allows studies to reveal the start-peak-decay patterns of bloom events. This may be helpful regarding taking preemptive measures for both environmental and economic purposes. Complimentary datasets, including the addition of routine *in-situ* radiometric measurements during a bloom event in addition to observing meteorological parameters and atmospheric conditions for the validation of satellite derived products would definitely improve the current proposed methods in this study. Additionally, with the rise of unmanned aerial systems (UAS) (drones, quadcopters, etc.) and the ever decreasing prices of smaller, handheld spectroradiometers, potential problems often encountered in satellite imagery could be eliminated. For example, a cloudy image over a target lake is useless, but a multi-spectral sensor attached to a UAS can provide a rapid assessment of the affected area and potentially derive preliminary concentration estimates.

Furthermore, spectral imaging or real-time RGB video from UAS relieves the need for an atmospheric correction, which resolves pre-processing time and frustration.

On the other hand, this free, robust multi-satellite based method can not only have a large impact on the proposed ongoing project conducted by UDEQ, but also for many other inland water bodies which face frequent CyanoHABs every summer as the warming trend continues. The satellite-based techniques proposed in this study can essentially be applied to any sensor that contains the required input bands after derived accurate R_{rs} values with the MAIN algorithm. Obviously, with the increasing frequency of CyanoHAB events across thousands of inland water bodies, the time and resources needed to validate every satellite overpass is incomprehensible. In the meantime, monitoring inland water quality using higher spatial resolution satellite imagery combined with widely accepted, traditional water quality algorithms developed in the past can provide a spatially accurate representation of the study area in addition to a quantitative, preemptive assessment at no expense.

REFERENCES

S. Adler-Golden, A. Berk, L.S. Bernstein, S. Richtsmeier, P. K. Acharya, M. W. Matthew, G. P. Anderson, C. L. Allred, L. S. Jeong, J. H. Chetwynd, FLAASH, a MODTRAN4 atmospheric correction package for hyperspectral data retrievals and simulations. In *Proc. 7th Ann. JPL Airborne Earth Science Workshop*, pp. 9-14, Dec., 1998

C. Ahn, A. Chung, H. Oh, Rainfall, phycocyanin, and N: P ratios related to cyanobacterial blooms in a Korean large reservoir. *Hydrobiologia*, 474*(1)*, pp. 117-124, Apr., 2002.

Y.H. Ahn, P. Shanmugam, J.H. Ryu, and J. Jeong, Satellite detection of harmful algal bloom occurrences in Korean waters, *Harmful Algae. 5(2)*, pp. 213–231, Mar., 2006.

D. Antoine, F. d'Ortenzio, S.B. Hooker, G. Bécu, B. Gentili, D. Tailliez, A. J. Scott, Assessment of uncertainty in the ocean reflectance determined by three satellite ocean color sensors (MERIS, SeaWiFS and MODIS-A) at an offshore site in the Mediterranean Sea (BOUSSOLE project), 113(C7), Jul., 2008.

Atech, Cost of algal blooms. Report to Land and Water Resources Research and Development Corporation, Canberra, ACT 2601 ISBN 0 642 76014 4, 2000.

S. W. Bailey, *and* P. J. Werdell, A multi-sensor approach for the on-orbit validation of ocean color satellite data products, *Remote Sensing of Environment*, 102(1), pp. 12-23, Jan., 2006.

S.W. Bailey, B. A. Franz, P. J. Werdell, Estimation of near-infrared water-leaving reflectance for satellite ocean color data processing, *Optics Express*, 18(7), pp. 7521-7527, Mar., 2010.

A. G. P. A. Berk, G. P. Anderson, P. K. Acharya, J. H. Chetwynd, L. S. Bernstein, E. P. Shettle, M. W. Matthew, S. M. Adler-Golden, MODTRAN4 user's manual, *Air Force Research Laboratory*, Hanscom AFB, MA, 1731, pp. 3010, 1999.

N. Bernardo, F. Watanabe, T. Rodrigues, E. Alcântara, Atmospheric correction issues for retrieving total suspended matter concentrations in inland waters using OLI/Landsat-8 image, *Advances in Space Research*, In press, Corrected Proof, Feb., 2017.

E. Mandanici *and* G. Bitelli, Preliminary Comparison of Sentinel-2 and Landsat-8 imagery for a combined use, *Remote Sensing* 8(12), pp. 1014, Sep., 2016

D. J. Carpenter, Modeling inland water quality using Landsat data, *Remote Sensing of Environment*, 13(4), pp. 345-352, Sept., 1983.

P. Chauhan, M. Mohan, S. Nayak, Comparative analysis of ocean color measurements of IRS-P4 OCM and SeaWiFS in the Arabian Sea, *IEEE transactions on geoscience and remote sensing*, 41(4), pp. 922-926, Jun., 2003.

P. S. Chavez Jr., An improved dark-object subtraction technique for atmospheric scattering correction of multispectral data, *Remote Sensing of Environment*, 24, pp. 459-479, 1988.

G. Dall'Olmo, A. A. Gitelson D. C. Rundquist, Towards a unified approach for remote estimation of chlorophyll-*a* in both terrestrial vegetation and turbid productive waters, *Geophysical Research Letters*, 30(18), Sep., 2003.

P. Dash, N. Walker, D. Mishra, E. D'Sa, S. Ladner, Atmospheric correction and vicarious calibration of Oceansate-1 Ocean Color Monitor (OCM) data in coastal Case-2 waters. *Remote Sensing*, 4(6), pp 1716-1740, Jun., 2012.

A. G. Dekker, Detection of the optical water quality parameters for eutrophic waters by high resolution remote sensing, *PhD Dissertation (Amsterdam) Free University*, 1993.

R. Doerffer, Imaging spectroscopy for detection of chlorophyll and suspended matter, GKSS-Forschungszentrum, 1992.

A. I. Dogliotti, K. G. Ruddick, B. Nechad, D. Doxaran, E. Knaeps, A single algorithm to retrieve turbidity from remotely-sensed data in all coastal and estuarine waters, *Remote Sensing of Environment*, 156, pp. 157-168, Jan., 2015.

D. S. Fisher, J. L. Steiner, D. M. Endale, J. A. Stuedemann, H.H. Schomberg, A. J. Franzluebbers, S. R. Wilkinson, The relationship of land use practices to surface water quality in the Upper Oconee Watershed of Georgia, *Forest Ecology and Management*, 128, pp. 39-48, Sep., 1999.

B. A. Franz, S. W. Bailey, N. Kuring, P. J. Werdell, Ocean Color Measurements from Landsat-8 OLI using SeaDAS, 2014.

A. A. Gilerson, A. A. Gitelson, J. Zhou, D. Gurlin, W. Moses, I. Ioannou, S. a. Ahmed, Algorithms for remote estimation of chlorophyll-*a* in coastal and inland waters using red and near infrared bands, *Optics Express*, 18(23), pp. 24109-24125, Nov., 2010.

H. R. Gordon, Ocean color remote sensing systems: radiometric requirements, *Proc. SPIE 0924, Recent Advances in Sensors, Radiometry and Data Processing for Remote Sensing*, 151, Oct., 1988.

H. R. Gordon, Atmospheric correction of ocean color imagery in the Earth Observing System era, *Journal of Geophysical Research: Atmospheres*, 102(D14), pp. 17081-17106, Jul., 1997.

H. R. Gordon *and* K. J. Voss, Modis Normalized Water-leaving Radiance, Algorithm Theoretical Basis Document (MOD 18), version 4, *NASA Contract Number NAS503163,* Apr., 1999.

H. R. Gordon *and* M. Wang, Retrieval of water-leaving radiance and aerosol optical thickness over the oceans with SeaWiFS: a preliminary algorithm, *Applied optics*, 33(3), pp. 443-452, Jan., 1994.

R. W. Gould Jr. *and* R. A. Arnone, Remote sensing estimates of inherent optical properties in a coastal environment, *Remote Sensing of Environment*, 61(2), pp. 290-301, Aug., 1997.

D.I. Greenfield, A. Duquette, A. Goodson, C.J. Keppler, S.H. Williams, L.M. Brock, Stackley, K.D. White and S.B. Wilde, The effects of three chemical algaecides on cell numbers and toxin content of the cyanobacteria Microcystis aeruginosa and Anabaenopsis sp. *Environmental management*, *54*(5), pp. 1110-1120, Nov., 2014.

J. E. Hansen *and L.* D. Travis, Light scattering in planetary atmospheres, *Space Science Reviews*, 16, pp. 527–610, May, 1974.

M. Hansson *and* B. Hakansson, The Baltic Algae Watch System - a remote sensing application for monitoring cyanobacterial blooms in the Baltic Sea, *Journal of Applied Remote Sensing*, 1(1):011507, Dec., 2007.

P. Härmä, J. Vepsäläinen, T. Hannonen, T. Pyhälahti, J. Kamari, K. Kallio, K. Eloheimo, S. Koponen, Detection of water quality using simulated satellite data and semi-empirical algorithms in Finland, *Science of the Total Environment*, 268(1), pp. 107-121, 2001.

X. He, Y. Bai, D. Pan, J. Tang, D. Wang, Atmospheric correction of satellite ocean color imagery using ultraviolet wavelength for highly turbid waters, *Optics express*, 20(18), pp. 20754-20770, Aug., 2012.

C. Hu, K. L. Carder, F. E. Muller-Karger, Atmospheric correction of SeaWiFS imagery over turbid coastal waters: a practical method. *Remote sensing of Environement*, 74(2), pp. 195-206, Nov., 2000.

C. Hu, Z. Chen, T. D. Clayton, P. Swarzenski, J. C. Brock, F. E. Muller-Karger, Assessment of estuarine water-quality indicators using MODIS medium-resolution bands: Initial results from Tampa Bay, FL, *Remote Sensing of Environment*, 93(3), pp. 423–441, Nov., 2004.

C. Hu, A novel ocean color index to detect floating algae in the global oceans, *Remote Sensing of Environment*, 113(10), pp. 2118-2129, May, 2009.

P.D. Hunter, A.N. Tyler, L. Carvalho, G.A. Codd and S.C. Maberly, Hyperspectral remote sensing of cyanobacterial pigments as indicators for cell populations and toxins in eutrophic lakes, *Remote Sens. Environ.*, 114*(11)*, pp. 2705-2718, Nov., 2010.

J. R. Irons, J. L. Dwyer, J. A. Barsi, The next Landsat satellite: The Landsat data continuity mission, *Remote Sensing of Environment*, 122, pp. 11-21, 2012.

R.H. Jackson, *and* D. J. Stevens, Physical and cultural environment of Utah Lake and adjacent areas, *Great Basin Naturalist Memoirs*, pp. 3-23, 1981.

C. Jamet, H. Loisel, C. P. Kuchinke, K. Ruddick, G. Zibordi, H. Feng, Comparison of three SeaWiFS atmospheric correction algorithms for turbid waters using AERONET-OC measurements, *Remote Sensing of Environment*, 115(8), pp. 1955-1965, Apr., 2011.

L. Jiang, *and* M. Wang, Improved near-infrared ocean reflectance correction algorithm for satellite ocean data processing, *Optics express*, 22(18), pp. 21657-21678, Sep., 2014.

D. L. Jupp, J.T. Kirk, G. P. Harris, Detection, identification and mapping of cyanobacteria – using remote sensing to measure the optical quality of turbid inland waters, *Marine and Freshwater Research*, 45(5), pp. 801-828, 1994.

I. Kanoshina *and* J. M. Leppänen, The influence of weather conditions (temperature and wind) on cyanobacterial bloom development in Gult of Finland (Baltic Sea), *Harmful Algae*, 2(1), pp. 29-41, Nov., 2002.

A. Koontz, C. Flynn, G. Hodges, J. Michalsky, and J. Barnard,Aerosol Optical Depth Value-Added Product, *US Department of Energy*, 32, Mar., 2013.

A. Kumar, D. R. Mishra, S. M. Equeenuddin, H. J. Cho, G. Rastogi, Differential Impact of Anniversary-Severe Cyclones on the Water Quality of a Tropical Coastal Lagoon, *Estuaries and Coasts*, 40(2), pp. 317-342, Mar., 2017.

G. E. Likens, Primary production of inland acquatic ecosystems, *Primary productivity of the biosphere*, Springer Berlin Heidelberg, pp., 185-202, 1975.

M. W. Matthew, S. M. Adler-Golden, A. Berk, S. C. Richtsmeier, R. Y. Levine, L. S. Bernstein, P. K. Acharya, G. P. Anderson, G. W. Felde, M. L. Hoke, A. J. Ratkowski, Statuts of atmospheric correction using a MODTRAN4-based algorithm, In *AeroSense 2000*, pp. 199-207, Aug, 2000.

J. McElhiney *and* L. A. Lawton, Detection of the cyanobacterial hepatotoxins microcystins, *Toxicology and Applied Pharmacology*, 203(3), pp. 219-230, Jul., 2004.

L. B. Meritt, Utah Lake: A few considerations, Utah Department of Environmental Quality, Mar., 2014.

D. R. Mishra, S. Narumalani, D. Rundquist, M. Lawson, Characterizing the vertical diffuse attenuation coefficient for downwelling irradiance in coastal waters: Implications for water penetration by high resolution satellite data, *ISPRS Journal of Photogrammetry & Remote Sensing*, 60(1), pp. 48-64, Nov., 2005.

S. Mishra *and* D. R. Mishra, Normalized difference chlorophyll index: A novel model for remote estimation of chlorophyll-*a* concentration in turbid productive waters, *Remote Sensing of Environment*, 117, pp. 394-406, 2011

S. Mishra, D. R. Mishra, W. M. Schlucter, A novel algorithm for predicting phycocyanin concentrations in cyanobacteria: A proximal hyperspectral remote sensing approach, *Remote Sensing*, 1(4), pp. 758-775, Oct., 2009.

S. Mishra, D. R. Mishra, Z. Lee, C. S. Tucker, Quantifying cyanobacterial phycocyanin concentration in turbid productive waters: A quasi-analytical approach, *Remote Sens. of Environ.*, 113, pp. 141-151, 2013.

C. D. Mobley, Estimation of the remote-sensing reflectance from above-surface measurements, *Applied Optics*, 38(36), pp. 7442-7455, Dec., 1999.

W. J. Moses, A. A. Gitelson, S. Berdnikov, V. Saprygin, V. Povazhnyi, Operational MERIS-based NIR-red algorithms for estimating chlorophyll-*a* concentrations in coastal waters – The Azov Sea case study, *Remote Sensing of Environment*, 121, pp. 118-124, Jan. 2012.

T. A. Msagati, B. A. Siame, D. D. Shushu, Evaluation of methods for the isolation, detection and quantification of cyanobacterial hepatotoxins, *Aquatic toxicology*, 78(4), pp. 382-397, Mar., 2006.

B. Nechad, K. G. Ruddick, Y. Park, Calibration and validation of a generic multisensor algorithm for mapping of total suspended matter in turbid waters, *Remote Sensing of Environment* 114(4), pp. 854-866, Nov., 2009.

J. E. O'Reilly, S. Maritorena, S. A. Siegel, M. C. O'Brien, D. Toole, B. G. Mitchell, M. Kharu, F. P Chavez, P. Strutton, G. F. Gota, S.B. Hooker, Ocean color chlorophyll algorithms for SeaWiFS, OC2, and OC4: Version 4, *SeaWiFS postlaunch calibration and validation analysis*, Part, 3, pp. 9-23, Jul., 2000.

J. Osswald, S. Relian, A. Gago, V. Vasconcelos, Toxicology and detection methods of the alkaloid neurotoxin produced by cyanobacteria, anatoxin-a, *Environment international*, 33(8), pp. 1070-1089, Nov., 2007.

C. Östlund, P. Flink, N. Strömbeck, D. Pierson, T. Lindell, Mapping of the water quality of Lake Erken, Sweden, from imaging spectrometry and Landsat Thematic Mapper, *Science of the Total Environment*, 268(1), pp. 139-154, Mar. 2001.

H. W. Paerl, *and* T. G. Otten, Harmful cyanobacterial blooms: causes, consequences, and controls, *Microbial ecology*, 65(4), pp. 995-1010, Dec., 2013

H.W. Paerl *and* V. J. Paul, Climate change: links to global expansion of harmful cyanobacteria. *Water Research*, 46(5), pp. 1349-1363, Aug., 2011.

H. W. Paerl, H. Xu, N. S. Hall, G. Zhu, B. Qin, Y. Wu, K. L. Rossignol, L. Dong, M. J. McCarthey, A. R. Joyner, Controlling cyanobacterial blooms in hypertrophic Lake Taihu, China: Will nitrogen reductions cause replacement of non-N2 fixing by N2 fixing taxa? *PLoSOne*, 9 (11), e113123, Nov., 2014.

D. C. Pierson *and* N. Strömbeck, A modelling approach to evaluate preliminary remote sensing algorithms: Use of water quality data from Swedish Great Lakes, *Geophysica*, 36(1-2), pp. 177-202, Oct., 2000.

K. Randolph, J. Wilson, L. Tedesco, L. Li, D. L. Pascual, E. Soyeux, Hyperspectral remote sensing of cyanobacteria in turbid productive water using optically active pigments, chlorophyll-*a* and phycocyanin. *Remote Sensing of Environment*, 112(11), pp. 4009-4019, Jun., 2008.

A. Reinart and T. Kuster, Comparison of different satellite sensors in detecting cyanobacterial bloom events in the Baltic Sea, *Remote Sens. of Environ.*, 102, pp. 74–85, Feb., 2006.

R. Richter, D. Schläpfer, Atmospheric/topographic correction for satellite imagery, DLR report DLR-IB 565-02/14, Wessling, Germany, Feb. 2014.

K. G. Ruddick, F. Ovidio, M. Rijkeboer, Atmospheric correction of SeaWiFS imagery for turbid coastal and inland waters, *Applied optics*, 39(6), pp. 897-912, Feb., 2000.

A. Ruiz-Verdú, S. G. Simis, C. de Hoyos, H. J. Gons, R. Peña-Martinez, An evaluation of algorithms for the remote sensing of cyanobacterial biomass, *Remote Sensing of Environment*, 112(11), pp. 3996-4008, Nov., 2007.

J. F. Schalles *and* Y. Z. Yacobi, Remote detection and seasonal patterns of phycocyanin, carotenoid and chlorophyll pigments in eutrophic waters, *Ergebnisse Der Limnologie*, 55, pp. 153-168, Feb., 2000

T. Schroeder, M. Schaale, J. Fischer, Retrieval of atmospheric and oceanic properties from MERIS measurements: A new Case-2 water processor for BEAM, *International Journal of Remote Sensing*, 28(24), pp. 5627-5632, Dec. 2007.

R. E. Sengpiel, Using airborne hyperspectral imagery to estimate chlorophyll a and phycocyanin in three central Indiana mesotrophic to eutrophic reservoirs, Doctoral dissertation, facult of the University Graduate School in partial fulfillment of the requirements for the degree of Master of Science in the Department of Earth Sciences, Indiana University), Aug., 2007.

D. A. Siegel, M. Wang, S. Maritorena, W. Robinson, Atmospheric correction of satellite ocean color imagery: the black pixel assumption, *Applied optics*, 39.21, pp., 3582-3591, Jul., 2000.

S. Simis, S. Peters, H. Gons, Remote sensing of the cyanobacterial pigment phycocyanin in turbid inland water, *Limnol. Oceanogr.* 50, pp. 237-245, Jan., 2005

M. E. Smith *and* K.M. Manoylov, Changes in Diatom Biodiversity in Lake Sinclair, Baldwin County, Gerogia, USA, *Journal of Water Resource and Protection*, 5(07), pp. 732-741, Jun., 2013.

M. Steffen, S.B. Watson, G.L. Boyer, S.W. Wilhelm, Status, causes and controls of cyanobacterial blooms in Lake Erie. *J. Great Lakes Res*., 40(2), pp. 215-225, Oct., 2014.

D. A. Steffensen, Economic cost of cyanobacterial blooms, In: Hudnell, H.K. (Ed.), *Cyanobacterial Harmful Algal Blooms: State of the Science and Research Needs*, pp. 855-865, 2008.

A. E. Strong, Remote sensing of algal blooms by aircraft and satellite in Lake Erie and Utah Lake, *Remote Sensing of Environment,* 3, pp. 99–107, Jan., 1974.

T. Suresh, E. Desa, A. Mascarenhas, S.G.P Matondkar, P. Naik, S. R. Nayak, Cross-calibration of IRS-P4 OCM Satellite Sensor, *Proceeding of SPIE*, Goa, India, 6404 pp. 1-9, Nov., 2006

R. M. Tyler, D.C. Brady, T.E. Targett, Temporal and spatial dynamics of diel-cycling hypoxia in estuarine tributaries, *Estuaries and Coasts,* 32, No. 1, pp. 123-145, Oct., 2008.

Q. Vanhellemont *and* K. Ruddick, Turbid wakes associated with offshore wind turbines observed with Landsat 8, *Remote Sensing of Enviornment*, 145, pp. 105-115, Apr., 2014.

Q. Vanhellemont *and* K. Ruddick, Advantages of high quality SWIR bands for ocean colour processing: Examples from Landsat-8. *Remote Sensing of Enviornment*, 161, pp. 89-106, May, 2015.

Q. Vanhellemont *and* K. Ruddick, ACOLITE for Sentinel-2: Aquatic Applications of MSI Imagery, In *Living Planet Symposium; Ouwehand, L. Ed.; ESA Communications: Noordwijk, The Netherlands*, Vol. 740, May, 2016.

E. F. Vermote, C. Justice, M. Claverie, B. Franch, Preliminary analysis of the performance of the Landsat 8/OLI land surface reflectance product, *Remote Sensing of Environment*, 185, pp. 46-56, Nov., 2016.

E. F. Vermote, D. Tanre, J. L. Deuze, M. Herman, J. J. Morcette, Second simulation of the satellite signal in the solar spectrum, 6S: An overview, *IEEE transactions on geoscience and remote sensing*, 35(3), pp. 675-686, May, 1997.

R. K. Vincent, X. Qin, R. M. L. McKay, J. Miner, K. Czajkowski, J. Savino, T. Bridgeman, Phycocyanin detection from LANDSAT TM data for mapping cyanobacterial blooms in Lake Erie, *Remote Sensing of Environment*, 89(3), pp. 381-392, Oct., 2003.

F. Vuolo, W. T. Ng, C. Atzberger, Smoothing and gap-filling of high resolution multi-spectral time series: Example of Landsat data, *International Journal of Applied Earth Observation and Geoinformation*, 57, pp. 202-213, May, 2017.

P. J. Werdell *and* S. Bailey, An improved in-situ bio-optical data set for ocean color algorithm development and satellite data product validation, *Remote sensing of environment*, 98(1), pp. 122-140, Jul., 2005.

H. Ye, C. Chen, C. Yang, Atmospheric correction of Landsat-8/OLI Imagery in Turbid Estuarine Waters: A Case Study for the Pearl River Estuary, *IEEE Journal of Selected Topics in Applied Earth Observatories and Remote Sensing*, 10(1), pp. 252-261, Oct., 2016\

D. Z. Zhao, X.G. Xing, Y.G. Liu, J.H. Yang, and L. Wang, The relationship of chlorophyll-a concentration with the reflectance peak near 700 nm in algae-dominated waters and sensitivity of fluorescence algorithms for detecting algal bloom, *International Journal of Remote Sensing*, 31, pp. 39–48, Jan., 2010.

APPENDIX A

LIST OF ACRONYMS (in alphabetical order)

AU: Astronomical unit

CCD: Cyanobacterial cell count

CDOM: Colored dissolved organic matter

Chl-*a*: Chlorophyll-*a*

cyanoHABs: Cyanobacterial harmful algal blooms

λ: Wavelength

d: Earth-sun distance

DN: Digital number

DOS: Dark Object Subtraction

DU: Dobson Unit

ESA: European Space Agency

EVI: Enhanced Vegetation Index

FAI: Floating Algal Index

FLAASH: Fast Line-of-sight Atmospheric Analysis of Hypercubes

F_o': Instantaneous extraterrestrial solar irradiance

L1C: Level-1C

L_r: Rayleigh radiance contribution

L_{rc} : Rayleigh-corrected radiance

L_t*: Top-of-atmosphere radiance corrected for ozone

L_{TOA}: Top-of-atmosphere radiance

LS8: Landsat-8

MAIN: Modified atmospheric correction for inland waters

MERIS: Medium Resolution Imaging Spectroradiometer

MODIS: Moderate Resolution Imaging Spectroradiometer

MSI: MultiSpectral Imager

NASA: National Aeronautics Space Administration

NDCI: Normalized Difference Chlorophyll Index

NDVI: Normalized Difference Vegetation Index

NIR: Near-infrared

NOAA: National Oceanographic and Atmospheric Administration

OACs: Optically-active constituents

OBPG: Ocean Biology Processing Group

OCM: Ocean Color Monitor

OLI: Operational Land Imager

P: Pressure

RGB: Red, Green, Blue

ROI: Region of interest

R_{rs}: Remote sensing reflectance

ρ_{rc}: Rayleigh-corrected reflectance

ρTOA: Top-of-atmosphere reflectance

ρ_{w}: Water-leaving reflectance

S2A: Sentinel-2A

SeaWiFs: Sea-Viewing Field-of-View Sensor

SNAP: Sentinel Application Platform

SWIR: Short-wave infrared

t: Transmittance

TOA: Top-of-atmosphere

UDEQ: Utah Department of Environmental Quality